Ph.D. Dissertation of Jiyeong Cho

Kinetic Modeling of Catalytic Reaction: Systems for Conversion of Light Hydrocarbons to Value-Added Chemicals

촉매 반응 시스템의 동역학 모델링: 경질 탄화수소로부터 고부가가치 화합물로의 전환에 관하여

August 2023

Graduate School of Engineering
Seoul National University
Chemical & Biological Engineering

Jiyeong Cho

Kinetic Modeling of Catalytic Reaction: Systems for Conversion of Light Hydrocarbons to Value-Added Chemicals

Advisor: Prof. Won Bo Lee

Submitting a Ph.D. Dissertation

August 2023

Graduate School of Engineering
Seoul National University

Chemical and Biological Engineering

Jiyeong Cho

Confirming the Ph.D. Dissertation written by
Jiyeong Cho
August 2023

Chair	김 도 희	(Seal)
Vice Chair	이 원 보	(Seal)
Examiner	남 재 욱	(Seal)
Examiner	강 종 헌	(Seal)
Examiner	박 명 준	(Seal)

Abstract

The conversion of light hydrocarbons to value-added chemicals has emerged as a pivotal domain within the broader field of sustainable and green chemistry. This transformation process, often carried out over a variety of specialized catalysts, offers a strategic approach to harnessing the untapped potential of abundant light hydrocarbon feedstocks such as methane, ethane, and propane.

Light hydrocarbons, generally derived from natural gas, refinery gases, and shale gas, are primarily composed of carbon and hydrogen. These low-cost, abundant, and energy-dense resources have traditionally been used as fuels. However, their transformation into value-added chemicals, including methanol, dimethyl ether (DME), benzene, toluene, and xylene (BTX), can significantly augment their economic value and contribute to the diversification of chemical feedstocks.

This transformation process is a key element of modern chemical engineering and represents a sustainable path towards a circular carbon economy. It not only provides a high-value outlet for under-utilized resources but also contributes to the reduction of greenhouse gas emissions. Furthermore, the chemicals derived from light hydrocarbons are key intermediates for a myriad of industrial applications, including the synthesis of plastics, solvents, and fuels, thereby extending the value chain of these feedstocks.

However, the conversion of light hydrocarbons to value-added chemicals is not without challenges. The reactions often involve complex kinetics, catalyst deactivation issues, and sensitivity to reaction conditions. It is, therefore, imperative to develop effective and efficient catalysts and to gain a deeper understanding of the reaction mechanisms. This will enable the design of more robust and efficient processes and thus contribute to the advancement of this important area of research.

This article aims to provide a comprehensive overview of the recent developments in the field of light hydrocarbon conversion to value-added chemicals, with a particular emphasis on the underlying reaction mechanisms, the role of catalysts, and strategies for addressing the associated challenges. We hope that this review will stimulate further innovation and research in this promising and rapidly evolving field.

This doctoral thesis combines the development of two comprehensive microkinetic models for chemical reactions of industrial importance: the conversion of syngas to dimethyl ether (DME) over a bifunctional catalyst (CZA/FER) and the synthesis of aromatic compounds (BTX) from ethane/propane over Ga/ZSM-5 with a focus on catalyst deactivation due to coking.

In the first part, a novel microkinetic model for DME synthesis from syngas via methanol over a CZA/FER hybrid catalyst is established. The model examines detailed reaction rates and site fractions, accounting for 28 reactions over CZA and nine reactions over FER, and reveals the dominance of the associative pathway for DME synthesis. Reaction parameters are determined using advanced theoretical approaches, and the pre-exponential factors of Arrhenius rate constants are estimated with experimental data. This model delineates a nuanced understanding of the catalytic reaction system, differing from previous research, and provides a viable operating condition range for CO2 conversion in the feed.

The second part presents a detailed kinetic model for the synthesis of BTX from ethane and propane over a Ga/ZSM-5 catalyst, considering both Langmuir adsorption kinetics and lumped oligomerization kinetics. The model includes the dynamics of coke accumulation, which leads to catalyst deactivation. Through a series of adsorption-driven reactions and oligomerization reactions, intermediates are formed, leading to BTX synthesis and coke formation. Experimental data over a wide temperature range and feed compositions validate the model predictions for the conversion of reactants and the yield of products.

Collectively, this thesis presents a comprehensive understanding of the catalyst role in these industrially significant reactions and the deactivation effects due to coke accumulation, thus enhancing our knowledge of the reaction kinetics and providing a theoretical foundation for optimizing these processes and designing more effective catalysts.

Keyword : Kinetic modeling, Catalytic conversion, Microkinetics, Deactivation of catalyst
Student Number : 2017-26418

Chapter 1. Introduction

1.1. Study Background

The transition towards sustainability and green energy practices is reshaping the chemical industry's focus towards the efficient utilization of resources. Specifically, the conversion of both synthetic gas, or syngas, into dimethyl ether (DME) via methanol and light hydrocarbons, such as ethane and propane, into value-added aromatic compounds (BTX) presents promising strategies that align with the principles of green chemistry and sustainable practices.

Syngas, a mixture of carbon monoxide, carbon dioxide, and hydrogen, can be efficiently converted into DME via methanol. This two-step process involves the catalytic conversion of syngas into methanol, followed by the dehydration of methanol to form DME. DME, with its wide-ranging applications, from aerosol propellants to clean-burning alternative fuel, exemplifies the concept of value-added products.

On the other hand, light hydrocarbons such as ethane and propane, which are abundant by-products of natural gas processing and petroleum refining, present a significant potential for the production of aromatic compounds including benzene, toluene, and xylene (BTX). Advanced catalysts, such as Ga/ZSM-5, have been successful in promoting the conversion of these light hydrocarbons into BTX, presenting an effective method to maximize the economic value of these resources.

The production of DME from syngas and the conversion of ethane and propane into BTX compounds both serve as pivotal examples of the circular carbon economy. By utilizing resources more efficiently, we minimize wasteful practices and greenhouse gas emissions while effectively 'recycling' carbon within the industry.

In the context of a green energy paradigm, researching efficient, economically viable, and environmentally friendly pathways for the conversion of syngas into DME via methanol and the transformation of light hydrocarbons into BTX represents a crucial research frontier. The advancements made in these areas will not only contribute to more sustainable industrial practices but will also play a significant role in addressing global environmental challenges.

1.2. Purpose of Research

Kinetic modeling plays a crucial role in the field of chemical engineering and catalysis, providing a comprehensive understanding of reaction pathways and the fundamental mechanisms that govern chemical transformations. It entails the development of mathematical descriptions to represent the progression of chemical reactions, aiding in the prediction of reaction rates and product distributions under various conditions. These models not only elucidate the underlying phenomena occurring at a molecular level but also inform the design and optimization of industrial chemical processes.

Kinetic models, notably those involving catalysis, typically incorporate various factors such as reactant adsorption, surface reaction, and desorption processes. In heterogeneous catalysis, for instance, these models must consider the nature of the catalyst and the interactions between the reactants and the catalyst surface. A significant aspect of these models is their ability to account for changes over time, including catalyst deactivation due to coke formation, a common challenge in many industrial processes.

Within the context of this study, kinetic modeling serves as a pivotal tool to shed light on the complex synthesis of aromatic compounds, specifically benzene, toluene, and xylene (BTX), from light hydrocarbons like ethane and propane over a Ga/ZSM-5 catalyst. Our kinetic model incorporates detailed reactions happening at the Lewis Acid Site (LAS) and the Brønsted Acid Site (BAS) of the catalyst, contributing to a deeper understanding of the processes involved. Moreover, it offers valuable insights into the long-term dynamics of the system, particularly the deactivation of the catalyst due to coke accumulation, a key concern in the sustainability and efficiency of the BTX synthesis process.

Through the proposed kinetic model, we aim to highlight the interconnectedness of the reactions, deactivation mechanisms, and the overall process performance. This will serve as a foundation for future work to improve and optimize the conversion of light hydrocarbons to BTX, an important set of compounds in the chemical industry.

1.3. Associated Publications

Part of Chapter 3, concerning the conversion of shale gas into DME over a CZA/FER hybrid catalyst, is based on the work of mine, “Microkinetic Study of Syngas Conversion to Dimethyl Ether over a Bifunctional Catalyst: CZA/FER”, accepted on *Korean Journal of Chemical Engineering* in July, 2023 and pertains to the microkinetic modeling of the integration of two distinct catalytic reaction systems. Part of Chapter 4, focusing on the conversion of ethane and propane into BTX over Ga/ZSM-5, has not been published yet, but it is being prepared for submission. It encompasses the modeling of an unknown catalytic reaction system based on experimental results and covers the topic of dynamic deactivation modeling throughout the progression of the catalytic reaction.

Chapter 2. Background Theory

2.1. Microkinetic modeling and lumped kinetic modeling

Microkinetic modeling and lumped (or simplified) kinetic modeling represent two contrasting approaches in the field of reaction kinetics, each with its unique advantages and application domains. Understanding these two modeling strategies is crucial for the study of catalytic reactions and the development of effective and efficient catalytic processes.

Microkinetic modeling is an approach that aims to model the detailed elementary reaction steps occurring on a catalyst surface. It is based on the understanding of individual reaction steps at the molecular level, including adsorption, surface reaction, and desorption processes. Each of these steps is characterized by its rate constant and activation energy. This approach can provide detailed insights into the mechanistic aspects of a catalytic process and allows for the prediction of reaction rates under various conditions. Microkinetic models can capture the complexity of the catalytic system, including the coverage effects, the effect of adsorbate-adsorbate interactions, and the influence of various reaction intermediates. However, microkinetic modeling can be computationally intensive and requires a comprehensive understanding of the reaction mechanism, making it less suitable for systems with poorly understood or highly complex mechanisms.

On the other hand, lumped kinetic modeling represents a more simplified approach where multiple elementary reaction steps are combined or "lumped" into a single reaction step. The primary goal of lumped kinetic modeling is to capture the overall behavior of the system rather than detailing each reaction step. The main advantage of this approach is its simplicity and computational efficiency. It can provide a practical framework for designing and optimizing catalytic processes, especially when detailed mechanistic information is lacking, or the reaction network is too complex. However, it's worth noting that the simplification in lumped kinetic models often comes at the expense of losing mechanistic insights into the reaction system.

In conclusion, the choice between microkinetic and lumped kinetic modeling depends on the specific requirements of the study. While microkinetic modeling offers more detailed insights into reaction mechanisms, lumped kinetic modeling can provide a simpler and more computationally efficient tool for predicting overall reaction rates and guiding process design and optimization. Both approaches are important tools in the arsenal of a researcher studying catalytic reactions, and understanding their respective strengths and limitations is critical for effective application.

2.2. Langmuir adsorption model

The Langmuir adsorption model, developed by Irving Langmuir in 1918, is a fundamental and widely used model in physical chemistry that explains the process of adsorption of molecules on solid surfaces. It provides a theoretical framework that quantitatively describes the interaction of gas molecules with a solid surface and forms the foundation for understanding the behaviors of catalysts in many chemical processes.

The model is based on several key assumptions. Firstly, it posits that the surface of the adsorbent has a finite number of identical sites, each of which is capable of binding one adsorbate molecule. Secondly, the model assumes that there are no interactions between the adsorbate molecules on adjacent sites. This implies that the adsorption on one site does not influence the adsorption on a neighboring site. Thirdly, it suggests that adsorption and desorption rates are dynamic processes which depend on the pressure of the adsorbate and surface coverage.

The Langmuir model is valuable due to its ability to mathematically describe the relationship between the concentration (or pressure) of the adsorbate in the gas phase and the extent of adsorption. It describes how the fraction of the adsorption sites occupied changes with changes in gas phase concentration, leading to an adsorption isotherm. The model yields a characteristic curve (Langmuir isotherm), which shows saturation at high concentrations or pressures of the adsorbate, a feature observed in many real systems.

Although the Langmuir adsorption model's assumptions may seem overly simplistic for some complex systems, it often provides a good first approximation for many surface adsorption processes, including heterogeneous catalysis, where the interaction between reactants and catalyst surface is a crucial step. Understanding the Langmuir model is crucial for designing and interpreting experiments involving surface processes, and for developing more sophisticated models that consider multiple adsorption sites, lateral interactions, or the heterogeneity of real surfaces.

2.3. The Arrhenius equation and transition state theory (TST)

The kinetic parameters were calculated in the form of the Arrhenius equation.

$$k_{AB} = A_{AB} * e^{\frac{-E_a}{k_B T}}$$

The pre-exponential factors (A_{AB}) were derived from transition state theory (TST), which provides a qualitative explanation for the relationship between chemical reactions and molecular structures based on collision theory. TST assumes a quasi-equilibrium between reactants, activated complexes, and products. In TST, the kinetic parameter for the forward reaction is related to the equilibrium constant for the formation of the activated complex. Based on TST, the values of A_{AB} for molecular adsorption and dissociative adsorption were set on the order of 10^1 $Pa^{-1}s^{-1}$, while those for molecular desorption and associative desorption were set on the order of 10^{13} s^{-1}. The initial values for the pre-exponential factors of the Langmuir-Hinshelwood surface reactions were set on the order of 10^{13} s^{-1} as in our previous research [1],[2]

2.4. Calculation of activation energy: UBI-QEP method and MP2 Calculation

Determining the base set of activation energy is extremely crucial in the process of conducting microkinetic modeling. This is because the fundamental aspects of the reaction at a specific temperature are decided based on the value of the activation energy. In most cases, activation energy is re-estimated based on experimental values, hence making the determination of the base set used for estimation significantly important in creating a microkinetic model.

The experimental values used for microkinetic modeling of the CZA/FER hybrid catalytic system discussed in Chapter 3 were measured at a single temperature, which can be seen as having relatively low sensitivity to activation energy. This system comprises a total of 72 forward and reverse reactions, including 35 reversible reactions and 2 irreversible reactions, making it computationally expensive to conduct ab-initio based calculations. Therefore, for 28 reactions on the CZA catalyst, we used the activation energy based on the unity bond index−quadratic exponential potential (UBI-QEP) method from our previous study with Park et al[3], [4] For the nine reactions on the FER catalyst, we used the activation energy calculated by Park et al. based on the second-order Møller-Plesset perturbation theory (MP2) calculations method which has been used in previous research with Park et al. also.

The UBI-QEP method is a semiempirical methodology for calculating the activation energies based simply on the adsorption energy (Q), the enthalpy of the reaction (ΔH_{rxn}), and the bond index (Φ). It assumes that two-body interactions in a multi-body system can be described as a quadratic potential of the exponential function of the two-center bond distance, similar to the bond index. By using this method, activation energies can be calculated using the enthalpies of the gas-species, the adsorption energies of the surface intermediates, and the bond indices of all of these with minimal computational burden.[3] Therefore, the method was applied to calculate the activation energies of the 28 forward and backward reactions over CZA.

MP2 method, which is used in the FER zeolite system, is a calculation methodology that accounts for electron correlation effects, making it well-suited to describe dispersion interactions [5], despite its high computational cost. Since the catalytic transformation of hydrocarbons over zeolites involves bond rearrangements and van-der-Waals interactions, it is important to consider the dispersion interactions of zeolites. To this end, we conducted MP2 calculations for a 4T cluster model of FER in our study. [1],[3]

2.5. Parameter estimation

Kinetic parameter estimation is a critical step in the development of kinetic models, which are mathematical representations of chemical reactions. These parameters, such as rate constants and activation energies, are essential for accurately predicting the behavior of a system under various conditions. The process of estimating these parameters often involves comparing model predictions with experimental data, a process known as model fitting or data fitting.

In the context of kinetic modeling, the goal is to adjust the parameters of the model so that the predicted behavior closely matches the observed experimental data. This is typically achieved through an iterative process, where the parameters are adjusted, the model predictions are recalculated, and the difference between the model predictions and the experimental data (the error) is quantified. This process is repeated until the error is minimized, indicating that the model predictions closely match the experimental data.

The quality of the parameter estimation and the resulting model predictions can be influenced by several factors. These include the quality and quantity of the experimental data, the complexity of the reaction mechanism, and the mathematical techniques used for parameter estimation. It's also important to consider the uncertainty in the parameter estimates, as this can impact the reliability of the model predictions.

In conclusion, kinetic parameter estimation is a crucial aspect of kinetic modeling, enabling the translation of experimental observations into predictive mathematical models. This process requires careful consideration of the experimental data, the reaction mechanism, and the parameter estimation techniques to ensure the development of reliable and accurate kinetic models.

Chapter 3. Microkinetic Modeling of Dimethyl Ether Synthesis from Synthetic Gas via Methanol over CZA/FER Hybrid Catalyst

3.1. Background

Dimethyl ether (DME) has garnered increasing attention as an environmentally friendly compound which does not contribute to global warming or produce NOx, SOx, or particulate matter (PM). It is an economical alternative fuel to diesel due to its high oxygen content, high cetane number, and lack of C-C bonds. Additionally, DME can be converted into various olefin products as a vital intermediate, making it a promising compound for future use.[6], [7]

There are two primary methods for synthesizing DME, the first of which involves the dehydration of methanol (MeOH) to produce DME and water, catalyzed by solid acid catalysts such as alumina, silica, or zeolites. The second method involves methane partial oxidation, where methane is oxidized to formaldehyde via MeOH, which is then converted to DME using a catalyst such as copper, silver, or platinum.[6] However, the majority of studies have focused on the dehydration of MeOH as the most effective method for synthesizing DME. The catalysts used for MeOH dehydration are typically acidic and include γ-Al_2O_3, Al_2O_3 with silica/phosphorus, and zeolites.[8], [9] This reaction is carried out under low pressure of up to 18 bar and temperatures ranging from 250 to 400℃, resulting in high selectivity towards DME and low coke formation.[10] Meanwhile, MeOH, which is used as a precursor for DME, is mainly synthesized through partial oxidation of syngas, a mixture of methane or CO and H_2. Commercially, syngas conversion to MeOH is carried out using copper-zinc-aluminum oxide (CZA) or iron-chromium oxide catalysts[11] Although the CZA catalyst is recognized for its high selectivity, its remarkable activity results in the formation of by-products, such as formaldehyde, formic acid, and formate, alongside CO_2 and H_2O, during the hydrogenation of CO and CO_2.[11]–[13]

The conversion of syngas to DME using catalytic methods has been extensively studied. The process can be divided into two steps, namely syngas to MeOH conversion and dehydration. The first step involves CO and CO_2 hydrogenation reactions and water gas shift (WGS) reactions. As the hydrogenation reactions occur widely, the syngas to MeOH conversion generates many intermediates and by-products.[11] The second step involves the product of the first step, i.e., MeOH. Commercial catalysts used for direct synthesis of DME from syngas typically comprise two functionally independent catalysts, namely Cu or Zn-based catalysts for CO and CO_2 hydrogenation and WGS reaction, and zeolite catalysts, which are known for their high selectivity, stability, and resistance to poisoning. [13]–[17]

The detailed mechanisms of each reaction are as follows. The CO and CO_2 hydrogenation and WGS reactions for synthesizing MeOH from syngas primarily use Cu-based catalysts under gas phase conditions, with the $Cu/ZnO/Al_2O_3$ catalyst, also known as CZA, being the most widely used catalyst. The kinetics of MeOH synthesis in the CZA system have been investigated by many researchers. In particular, Graaf et al. developed a lumped kinetic model for MeOH synthesis using a spinning basket reactor with CZA catalyst and successfully reproduced experimental data for CO and CO_2 hydrogenation at 15-50 bar and 483.15-518.15 K.[18]–[21] Furthermore, the chemical equilibrium of the WGS reaction in a fixed-bed reactor with CZA catalyst was simulated using the Soave-Redlich-Kwong equation of state at 10-80 bar and 473.15-543.15 K. However, lumped kinetic models are limited in their ability to show the details of the elementary reactions.

Several researchers[3], [6], [7], [16], [22]–[24] have studied the synthesis processes of MeOH and DME. Their studies can be divided into lumped kinetics or microkinetics. Lumped kinetics is a method of modeling the overall reaction rather than each elementary step reaction, and it is performed by assuming a rate-determining step. In contrast, microkinetic modeling is a method of modeling all possible elementary step reactions without assuming RDS, and it is usually performed for systems for which there is insufficient information on the catalyst for lumped kinetic modeling. The microkinetic model is used for the purpose of analyzing and understanding the catalyst system.[25] It allows us to take a look at the detailed information about the system such as rate controlling, equilibrated species and dominant surface species, etc. Also, it can be used as a reference model for lumped kinetics, which needs some information for the assumptions to be derived. Several computational methods were used to find thermodynamically favorable reactions from a reaction parameter perspective of an unknown catalytic reaction system. The most favorable reaction was estimated based on the activation energy and Gibbs free energy at each elementary step calculated using ab initio quantum chemistry methods such as Density Functional Theory.[25], [26] However, there is a limitation of evaluating the kinetically favorable reaction path because the concentration of the reactant, which is an important factor of the reaction kinetic system was not considered. To solve this problem, various microkinetics with the direct use of the Arrhenius equations were carried out. The microkinetic model was composed of the reaction rate equations of each elementary step using both the activation energy that reflects the thermodynamic effect and the concentration that reflects the kinetic effect. Karakaya et al.[27] introduced the site coverage fraction on the catalytic surface for modeling. Methane dehydroaromatization on Mo/Zeolite catalyst was simulated and analyzed using microkinetic modeling composed of 50 elementary steps. The same research team later performed microkinetic studies on

Mo/HZSM-5 catalyst using the site fraction of the Molybdenum site and the zeolite site of the bifunctional catalyst.[28] Similarly, Baz et al.[29] utilized a microkinetic model of the CO electro-oxidation reaction extended to two site types, Pt and alloy, to understand the bifunctional activity of the catalyst. Such research exemplifies microkinetic modeling utilizing reaction kinetic parameters that reflect the thermodynamic effects of each part of the bifunctional catalyst.

The MeOH dehydration over FER consists of approximately 10 elementary steps. Initially, the γ-Al_2O_3 catalyst was commonly used as an acidic dehydration catalyst. It adsorbs and dehydrates MeOH molecules, and converts them into DME.[30] Aguayo et al.[12] demonstrated a bifunctional catalyst to convert CO, CO_2, and H_2 feed into DME using CZA/γ-Al_2O_3 in 2007. Recently, zeolites have become the preferred catalyst for dehydrating MeOH because of its resistance for deactivation by coke accumulation.[10] Kubelková et al.[31] suggested that MeOH adsorbs to the active site of zeolite when MeOH hydration begins. Blaszkowski and van Santen[32], [33] divided the reaction into three pathways, including the associative and dissociative paths at the H-site of zeolite[32]. Based on DFT calculations, they claimed the dominance of the associative path. Conversely, there exists the opposing view that the dissociative path is dominant.[23], [34], [35] Jones and Iglesia[34], [35] argued that the dominance of the two paths is not absolute and depends on the conditions, particularly at high temperature and low pressure where the dissociative path is dominant. Similarly, Moses and Nørskov[23] claimed the dominance of the dissociative path based on DFT and relative reaction rate calculations. However, Carr et al.[36], based on reaction kinetic measurement and DFT calculations at 433 K, argued that medium and large size zeolites are not inhibited in high-pressure conditions, while small-pore zeolites are inhibited in dehydration to DME, due to the clustering effect of MeOH. Di Iorio et al.[7] studied the inhibition of MeOH dehydration to DME for zeolites with different pore sizes in high-pressure conditions where the partial pressure of MeOH is above 10 kPa and claimed that the associative path is thermodynamically dominant at high MeOH partial pressures due to the conjugation stabilization effect of MeOH. Generally, it is known that the dissociative path is dominant at temperatures above 500 K and pressures below 10 kPa, while the associative path is dominant at relatively low temperatures below 500 K and pressures above 10 kPa. However, it can vary depending on the specific conditions of the reaction system.

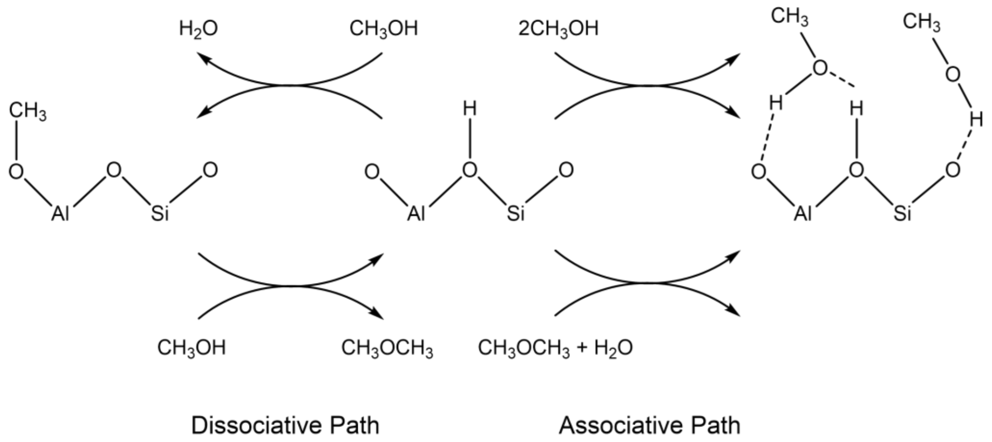

Figure 1 Dissociative and associative path in MeOH dehydration over FER

In summary, although the FER system comprises a relatively small number of reactions, microkinetic analysis can still be applied to the CZA system since it contains a significant number of possible elementary-step reactions. There were some earlier studies that construct the kinetic model of the bifunctional catalyst with two different active sites for each reactant[12], [16] but there were no studies for the microkinetic modeling of CZA/FER hybrid bifunctional catalyst. The microkinetic modeling for bifunctional catalysts can provide a variety of information about CZA/FER system and can compare those with the previous results of CZA[1] and FER[3] each. In this study, a microkinetic model for the CZA/FER hybrid bifunctional catalytic system is developed to investigate how the disputed HCOO** and COOH* intermediates in the CZA system affect the reaction patterns, how the CO_2 conversion differs depending on the hydrogen ratio in the feed and which elementary-step reactions are influenced by it, and how the competition between the associative and dissociative paths in the FER system changes.

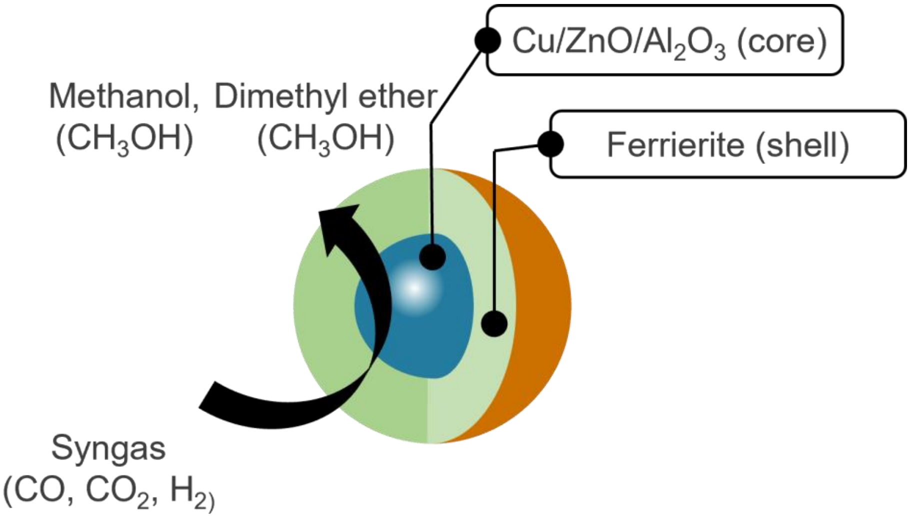

Figure 2 Core-shall structure of CZA/FER hybrid catalyst

3.2. Microkinetic Model and Reaction Mechanism

The microkinetic model comprises 28 reactions over CZA and nine reactions over FER. The CZA reactions include six adsorption/desorption reactions, while the FER reactions include three adsorption/desorption reactions. The remaining reactions in both cases are surface reactions. The rate equations for each type of reaction are provided below.

Adsorption reactions

$$r_i = k_i * \theta_{vacant} * P_i, k = A$$

Desorption reactions

$$r_i = k_i * \theta_i, k = A$$

Surface reactions

$$r_i = k_i * \theta_i, k = S_{c,i} * e^{\frac{-E_{a,i}}{RT}}$$

Chemical master equation

$$\frac{dy_i}{dy} = \frac{y_{i-1} - y_i}{\tau} + \sum_j r_j \dot{v}, \frac{dy_i}{dt} \rightarrow 0$$

θ_i, which represents the surface coverage for species i, were designated in each CZA and FER individually, and the site balance was constructed to satisfy $\sum \theta_{i,CZA} = 1$ and $\sum \theta_{i,FER} = 1$.

The reaction mechanism for DME synthesis from syngas via MeOH consists of the following overall reactions:

CO hydrogenation

$CO(g) + 2\ H_2(g) \leftrightarrow CH_3OH$

CO_2 hydrogenation

$CO_2(g) + 3\ H_2(g) \leftrightarrow CH3OH(g) + H2O(g)$

WGS reaction

$H_2O(g) + CO(g) \leftrightarrow H_2(g) + CO_2(g)$

MeOH dehydration

$2CH_3OH(g) \leftrightarrow CH_3OCH_3(g) + H_2O(g)$

The first three reactions produce MeOH from syngas over CZA, and Grabow et al.[11] proposed 49 elementary reactions for the production of the adsorbed form of MeOH, CH_3OH*, including the formation of other possible hydrogenated compounds such as HCO*, HCOO**, CH_2O*, COOH*, H_2COO*, CH_3O*, CH_3OO*, and $HCOOCH_3$*. The reaction system also includes gas-phase species absorbed on the surface such as CO*, CO_2*, H*, H_2O*, OH*, and CH_2O*. 28 elementary-step reactions were selected from these by neglecting undetected gas-phase species like HCOOH(g) and $HCOOCH_3$(g), and their surface intermediates.[1] (Reactions 1-28 in Table 1).

The fourth overall reaction, the MeOH dehydration reaction, produces DME over FER, based on the two specific paths: associative and dissociative. Computational chemistry analyses have suggested elementary-step reactions. (Reactions 29-37 in Table 1) [3], [23], [32]–[34]. Reaction 29 is the adsorption of MeOH to FER and is a starting step for both paths. Reactions 30-34 constitute the dissociative path, with CH_3-Z as an intermediate, whereas reactions 35-37 are the associative path, with CH_3OH-CH_3OH-H-Z as an intermediate.

Table 1 Table 1 Overall reaction mechanism of CZA/FER hybrid catalyst

No.	Reaction	r_f	r_b	Reaction Type
R1	$CO + * \leftrightarrow CO*$	$r_{f1}P_{CO}\theta_{Cu}$	$r_{b1}\theta_{CO}$	Adsorption /desorption reactions over a CZA
R2	$CO_2 + * \leftrightarrow CO_2*$	$r_{f2}P_{CO_2}\theta_{Cu}$	$r_{b2}\theta_{CO_2}$	
R3	$H_2 + 2* \leftrightarrow 2H*$	$r_{f3}P_{H_2}\theta_{Cu}$	$r_{b3}\theta_{H_2}$	
R4	$H_2O + * \leftrightarrow H_2O*$	$r_{f4}P_{H_2O}\theta_{Cu}$	$r_{b4}\theta_{H_2O}$	
R5	$CH_2O + * \leftrightarrow CH_2O*$	$r_{f5}P_{CH_2O}\theta_{Cu}$	$r_{b5}\theta_{CH_2O}$	
R6	$CH_3OH + * \leftrightarrow CH_3OH*$	$r_{f6}P_{CH_3OH}\theta_{Cu}$	$r_{b6}\theta_{CH_3OH}$	
R7	$CO* + O* \leftrightarrow CO_2* + *$	$r_{f7}\theta_{CO}\theta_{O}$	$r_{b7}\theta_{CO_2}\theta_{Cu}$	Surface reactions over a CZA
R8	$CO* + OH* \leftrightarrow COOH* + *$	$r_{f8}\theta_{CO}\theta_{OH}$	$r_{b8}\theta_{COOH}\theta_{Cu}$	
R9	$CO_2* + H* \leftrightarrow COOH* + *$	$r_{f9}\theta_{CO_2}\theta_{H}$	$r_{b9}\theta_{COOH}\theta_{OH}$	
R10	$CO_2* + H_2O* \leftrightarrow COOH* + OH*$	$r_{f10}\theta_{CO_2}\theta_{OH}$	$r_{b10}\theta_{COOH}\theta_{OH}$	
R11	$H_2O* + * \leftrightarrow OH* + H*$	$r_{f11}\theta_{H_2O}\theta_{Cu}$	$r_{b11}\theta_{OH}\theta_{H}$	
R12	$OH* + * \leftrightarrow O* + H*$	$r_{f12}\theta_{OH}\theta_{Cu}$	$r_{b12}\theta_{O}\theta_{H}$	
R13	$2OH* \leftrightarrow H_2O* + O*$	$r_{f13}\theta_{OH}^2$	$r_{b13}\theta_{H_2O}\theta_{O}$	
R14	$CO_2* + H* \leftrightarrow HCOO**$	$r_{f14}\theta_{CO_2}\theta_{H}$	$r_{b14}\theta_{HCOO}$	
R15	$HCOO** + H* \leftrightarrow H_2COO* + 2*$	$r_{f15}\theta_{HCOO}\theta_{H}$	$r_{b15}\theta_{H_2COO}\theta_{Cu}^2$	
R16	$H_2COO* + H* \leftrightarrow CH_3O_2* + *$	$r_{f16}\theta_{H_2COO}\theta_{H}$	$r_{b16}\theta_{CH_3O_2}\theta_{Cu}$	
R17	$H_2COO* + * \leftrightarrow CH_2O* + O*$	$r_{f17}\theta_{H_2COO}\theta_{Cu}$	$r_{b17}\theta_{CH_2O}\theta_{O}$	
R18	$CH_3O_2* + * \leftrightarrow CH_2O* + OH*$	$r_{f18}\theta_{CH_3O_2}\theta_{Cu}$	$r_{b18}\theta_{CH_2O}\theta_{OH}$	
R19	$CH_2O* + H* \leftrightarrow CH_3O* + *$	$r_{f19}\theta_{CH_2O}\theta_{H}$	$r_{b19}\theta_{CH_3O}\theta_{Cu}$	
R20	$CH_3O* + H* \leftrightarrow CH_3OH* + *$	$r_{f20}\theta_{CH_3O}\theta_{H}$	$r_{b20}\theta_{CH_3OH}\theta_{Cu}$	
R21	$CO* + H* \leftrightarrow HCO* + *$	$r_{f21}\theta_{CO}\theta_{H}$	$r_{b21}\theta_{HCO}\theta_{Cu}$	
R22	$HCOO** \leftrightarrow HCO* + O*$	$r_{f22}\theta_{HCOO}$	$r_{b22}\theta_{HCO}\theta_{O}$	
R23	$HCO* + H* \leftrightarrow CH_2O* + *$	$r_{f23}\theta_{HCO}\theta_{H}$	$r_{b23}\theta_{CH_2O}\theta_{Cu}$	
R24	$CO* + OH* \leftrightarrow HCO* + O*$	$r_{f24}\theta_{CO}\theta_{OH}$	$r_{b24}\theta_{HCO}\theta_{O}$	
R25	$CO* + H_2O* \leftrightarrow HCO* + OH*$	$r_{f25}\theta_{CO}\theta_{H_2O}$	$r_{b25}\theta_{HCO}\theta_{OH}$	
R26	$CH_3O* + CO* \leftrightarrow CH_2O* + HCO*$	$r_{f26}\theta_{CH_3O}\theta_{H}$	$r_{b26}\theta_{CH_2O}\theta_{HCO}$	
R27	$CH_3O* + HCO* \leftrightarrow CH_3OH* + CO*$	$r_{f27}\theta_{CH_3O}\theta_{HCO}$	$r_{b27}\theta_{CH_3OH}\theta_{CO}$	
R28	$CH_3O_2* + H* \leftrightarrow CH_2O* + H_2O*$	$r_{f28}\theta_{CH_3O_2}\theta_{H}$	$r_{b28}\theta_{CH_2O}\theta_{H_2O}$	
R29	CH_3OH (g) + HZ ↔ CH_3OH-HZ	$r_{f29}P_{CH_3OH}\theta_{H-Z}$	$r_{b29}\theta_{CH_3OH-H-Z}$	Surface reactions over a FER
R30	CH_3OH-HZ ↔ H_2O-CH_3-Z	$r_{f30}\theta_{CH_3OH-H-Z}$	$r_{b30}\theta_{H_2O-CH_3-Z}$	
R31	H_2O-CH_3-Z → CH_3-Z + H_2O (g)	$r_{f31}\theta_{H_2O-CH_3-Z}$	-	
R32	CH_3-Z + CH_3OH (g) ↔ CH_3OH-CH_3-Z	$r_{f32}P_{CH_3OH}\theta_{CH_3-Z}$	$r_{b32}\theta_{CH_3OH-CH_3-Z}$	
R33	CH_3OH-CH_3-Z ↔ CH_3OCH_3-HZ	$r_{f33}\theta_{CH_3OH-CH_3-Z}$	$r_{b33}\theta_{CH_3OCH_3-H-Z}$	
R34	CH_3OCH_3-HZ ↔ CH_3OCH_3 (g) + HZ	$r_{f34}\theta_{CH_3OCH_3-H-Z}$	$r_{b34}\theta_{CH_3OCH_3}\theta_{H-Z}$	
R35	CH_3OH-HZ + CH_3OH (g) ↔ CH_3OH-CH_3OH-HZ	$r_{f35}P_{CH_3OH}$ $*\,\theta_{CH_3OH-H-Z}$	r_{b35} $*\,\theta_{CH_3OH-CH_3OH-H-Z}$	
R36	CH_3OH-CH_3OH-HZ ↔ CH_3OCH_3-H_2O-HZ	r_{f36} $*\,\theta_{CH_3OH-CH_3OH-H-Z}$	r_{b36} $*\,\theta_{CH_3OCH_3-H_2O-H-Z}$	
R37	CH_3OCH_3-H_2O-HZ → HZ + CH_3OCH_3 (g) + H_2O (g)	r_{f37} $*\,\theta_{CH_3OCH_3-H_2O-H-Z}$	-	

The CZA catalytic reaction system consists of 28 reversible reactions, comprising a total of 56 elementary reactions of forward and reverse. Due to the high computational cost associated with performing ab-initio-based activation energy calculations in such a large reaction system, empirical equations such as the unity bond index-quadratic exponential potential(UBI-QEP) have been used in previous research.[1]

The UBI-QEP method is a semiempirical methodology for calculating the activation energies based simply on the adsorption energy (Q), the enthalpy of the reaction (ΔH_{rxn}), and the bond index (ϕ). It assumes that two-body interactions in a multi-body system can be described as a quadratic potential of the exponential function of the two-center bond distance, similar to the bond index. By using this method, activation energies can be calculated using the enthalpies of the gas-species, the adsorption energies of the surface intermediates, and the bond indices of all of these with minimal computational burden. Therefore, the method was applied to calculate the activation energies of the 28 forward and backward reactions over CZA.

In Table 2, the base parameter set over CZA catalyst for parameter estimation has been displayed.

Table 2 Base parameter set for parameter estimation: CZA

Reaction	A_f [s^{-1}]	A_b [s^{-1}]	E_f [eV]	E_b [eV]	bond index
R1	1.00E+00	1.00E+13	0.00	0.71	0.50
R2	1.00E+00	1.00E+13	0.00	0.04	0.50
R3	1.00E+00	1.00E+13	0.00	0.27	0.50
R4	1.00E+00	1.00E+13	0.00	0.18	0.50
R5	1.00E+00	1.00E+13	0.00	0.06	0.50
R6	1.00E+00	1.00E+13	0.00	0.19	0.50
Reaction	A_f [s^{-1}]	A_b [s^{-1}]	E_f [eV]	E_b [eV]	bond index
R7	1.00E+13	1.00E+13	1.62	0.53	0.95
R8	1.00E+13	1.00E+13	0.21	0.37	0.50
R9	1.00E+13	1.00E+13	0.00	0.52	0.95
R10	1.00E+13	1.00E+13	0.00	0.78	0.50
R11	1.00E+13	1.00E+13	0.81	0.55	0.50
R12	1.00E+13	1.00E+13	1.17	0.44	0.50
R13	1.00E+13	1.00E+13	0.61	0.14	0.95
R14	1.00E+13	1.00E+13	0.30	0.02	0.50
R15	1.00E+13	1.00E+13	0.20	1.09	0.50
R16	1.00E+13	1.00E+13	1.25	0.64	0.60
R17	1.00E+13	1.00E+13	0.76	0.00	0.50
R18	1.00E+13	1.00E+13	0.65	0.00	0.50
R19	1.00E+13	1.00E+13	0.98	0.01	0.50
R20	1.00E+13	1.00E+13	1.33	1.09	0.95
R21	1.00E+13	1.00E+13	0.00	0.72	0.50
R22	1.00E+13	1.00E+13	2.08	0.00	0.50
R23	1.00E+13	1.00E+13	0.62	0.19	0.50
R24	1.00E+13	1.00E+13	0.00	1.45	0.50
R25	1.00E+13	1.00E+13	0.00	0.98	0.50
R26	1.00E+13	1.00E+13	0.00	1.70	0.50
R27	1.00E+13	1.00E+13	0.00	0.96	0.50
R28	1.00E+13	1.00E+13	0.42	0.03	0.50

In the FER zeolite system, the activation energy was available in the previous study [3] where the second-order Møller-Plesset perturbation theory (MP2) calculations was applied. MP2 is a calculation methodology that accounts for electron correlation effects, making it well-suited to describe dispersion interactions, [5] despite its high computational cost. Since the catalytic transformation of hydrocarbons over zeolites involves bond rearrangements and [15] van-der-Waals interactions, it is important to consider the dispersion interactions of zeolites.

In Table 3, the base parameter set over FER catalyst for parameter estimation has been displayed and in Table 4, the operating conditions of the experiments are displayed.

Table 3 Base parameter set for parameter estimation: FER

Reaction	A_f [s^{-1}]	A_b [s^{-1}]	E_f [eV]	E_b [eV]
R29	1.00E+13	1.00E+13	0.000	0.751
R32	1.00E+13	1.00E+13	0.000	0.467
R35	1.00E+13	1.00E+13	0.000	0.243
Reaction	A_f [s^{-1}]	A_b [s^{-1}]	E_f [eV]	E_b [eV]
R30	1.00E+13	1.00E+13	2.876	2.769
R31	1.00E+13	1.00E+13	0.374	-
R33	1.00E+13	1.00E+13	2.669	2.914
R34	1.00E+13	1.00E+13	0.705	0.000
R36	1.00E+13	1.00E+13	2.509	2.770
R37	1.00E+13	1.00E+13	0.978	-

Table 4 Operating conditions of experimental run

Exp	T [°C]	P [bar]	GHSV [L/(kg$_{cat}$ h]	$CO/CO_2/H_2/N_2$ /[vol%]	$H_2/(2CO+3CO_2)$	Remarks
1	250	50	2000	21.0/6.0/66.0/4.0	0.96	Base case
2	250	20	2000	21.0/6.0/66.0/4.0	0.96	Pressure
3	250	30	2000	21.0/6.0/66.0/4.0	0.96	
4	250	40	2000	21.0/6.0/66.0/4.0	0.96	
5	250	50	4000	21.0/6.0/66.0/4.0	0.96	GHSV
6	250	50	6000	21.0/6.0/66.0/4.0	0.96	
7	250	50	8000	21.0/6.0/66.0/4.0	0.96	
8	250	50	2000	15.6/6.4/73.9/4.7	1.50	Feed Composition
9	250	50	2000	11.5/4.9/79.4/4.2	2.10	

To this end, we conducted MP2 calculations for a 4T cluster model of FER in our study. [3] Parameter estimation was performed using experimental data based on the operation result. The data were obtained from our previous work 13 (Table 3). There was a total of 12 experimental data under various temperatures, pressures, gas hourly space velocities (GHSV), and feed compositions. Among the 12 experimental data, three data for the temperature change were excluded because the activation energies of 72 elementary-step reactions was not estimated. The experimental conditions of the data are described in Table 4. The production rates of other byproducts like formaldehyde, formic acid, and light hydrocarbons containing methane, ethane, ethylene, etcwere neglected because their carbon-mole% in the experiment were less than 1%.

MATLAB (MathWorks, Inc.) was used as the primary platform, where the stiff ODE solver (ode15s) with the backward differentiation formula (BDF) algorithm was employed to solve the mass balance equations. Parameter estimation was conducted using the genetic algorithm (GA) to minimize the following objective function:

$$
\begin{aligned}
F_{\mathrm{obj}} = \sum_{i=1}^{9} \{ & WF_1[(X_{\mathrm{CO,calc}} - X_{\mathrm{CO,exp}})^2 + (X_{\mathrm{CO_2,calc}} - X_{\mathrm{CO_2,exp}})^2] \\
& + WF_2[(N_{\mathrm{CH_3OH,calc}} - N_{\mathrm{CH_3OH,exp}})^2 + (N_{\mathrm{CH_3OCH_3,calc}} - N_{\mathrm{CH_3OCH_3,exp}})^2]\}_i
\end{aligned}
$$

3.3. Result and Discussion

The estimated values of the pre-exponential factors are listed in Table 5. The CO and CO_2 conversions increased with increasing pressure (Exp1-4), while the increase of GHSV resulted in a decrease in conversion (Exp1, 5-7). The effects of hydrogen to carbon ratio (Exp8-9) on CO_2 conversion are particularly remarkable, indicating that CO_2 is consumed under the conditions of high H_2 composition. The simulated values of the four objective elements were normalized using the means and standard deviations of the experimental data, and the parity plot between raw data for 36 experimental and simulation data points is presented in the table 5 and figure 3.

The prediction results of MeOH/DME flow rates reflected the trend of the experimental values. Notably, MeOH production decreased with increasing hydrogen to carbon ratios, whereas DME production increased, indicating an accelerated adsorption reaction and promotion of the transformation to DME. In figure 10, the ratio of net reaction rates between Exp9 and Exp1 is presented that indicating with reaction 6, 29, 32 and 35, adsorption reactions of MeOH to catalyst, increased in Exp9 where the hydrogen to carbon ratio in feed increased than Exp1 where is the base case. However, the model's predicted values did not reflect the trend of experimental values of DME production rate with Exp1 and 8-9, the increasing in hydrogen to carbon ratio. Upon examining the experimental values under the given conditions, the CO conversion remains relatively constant, while the CO_2 conversion is increasing. Although the carbon conversion increases, the experimental data shows decreasing in both MeOH and DME synthesis. It may be the experimental error and the model's results, in which the MeOH production rate decreases and the DME production rate increases with the rise in carbon conversion, can be considered reasonable.

Table 5 Estimated parameter of CZA/FER hybrid catalytic system

Reaction	a [Pa^{-1}s^{-1}]		E_f [eV]	E_b [eV]
R1	3.20E-19		0.00	0.71
R2	3.35E-08		0.00	0.04
R3	1.55E-12		0.00	0.27
R4	8.77E-18		0.00	0.18
R5	5.15E-06		0.00	0.06
R6	1.10E-34		0.00	0.19
Reaction	A_f [s^{-1}]	A_b [s^{-1}]	E_f [eV]	E_b [eV]
R7	6.88E+16	1.00E+13	1.62	0.53
R8	1.19E+19	1.00E+13	0.21	0.37
R9	4.14E+06	1.00E+13	0.00	0.52
R10	6.37E+17	1.00E+13	0.00	0.78
R11	6.29E+11	1.00E+13	0.81	0.55
R12	6.85E+17	1.00E+13	1.17	0.44
R13	1.44E+11	1.00E+13	0.61	0.14
R14	4.52E+04	1.00E+13	0.30	0.02
R15	3.20E+18	1.00E+13	0.20	1.09
R16	2.86E+17	1.00E+13	1.25	0.64
R17	1.24E+17	1.00E+13	0.76	0.00
R18	1.25E+13	1.00E+13	0.65	0.00
R19	8.21E+05	1.00E+13	0.98	0.01
R20	1.06E+10	1.00E+13	1.33	1.09
R21	5.20E+07	1.00E+13	0.00	0.72
R22	1.67E+14	1.00E+13	2.08	0.00
R23	1.01E+13	1.00E+13	0.62	0.19
R24	9.38E+12	1.00E+13	0.00	1.45
R25	2.10E+19	1.00E+13	0.00	0.98
R26	7.54E+21	1.00E+13	0.00	1.70
R27	1.16E+06	1.00E+13	0.00	0.96
R28	1.36E+09	1.00E+13	0.42	0.03
Reaction	A_f [Pa^{-1}s^{-1}]	A_b [Pa^{-1}s^{-1}]	E_f [eV]	E_b [eV]
R29	3.55E+04	1.00E+13	0.000	0.751
R32	1.43E+07	1.00E+13	0.000	0.467
R35	1.00E+11	1.00E+13	0.000	0.243
Reaction	A_f [Pa^{-1}s^{-1}]	A_b [Pa^{-1}s^{-1}]	E_f [eV]	E_b [eV]
R30	1.00E+14	3.83E+13	2.876	2.769
R31	1.00E+18	-	0.374	-
R33	1.00E+11	3.46E+16	2.669	2.914
R34	1.00E+19	1.57E+03	0.705	0.000
R36	1.00E+22	3.01E+16	2.509	2.770
R37	1.00E+19	-	0.978	-

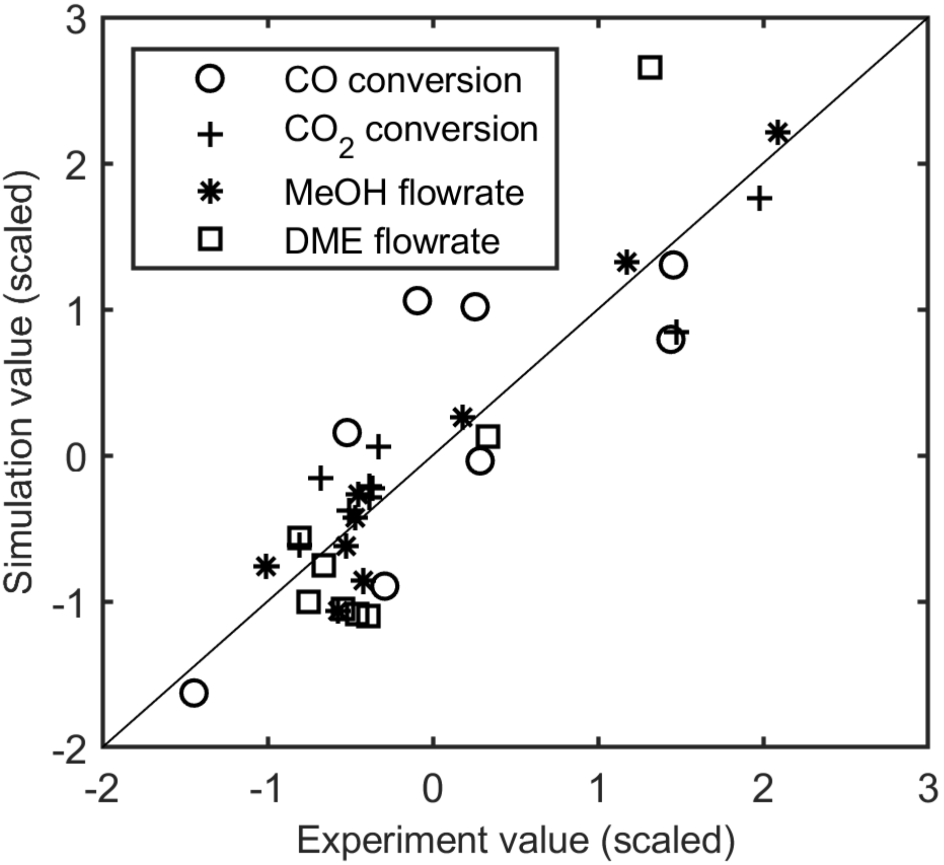

Figure 3 Parity plot of developed microkinetic model

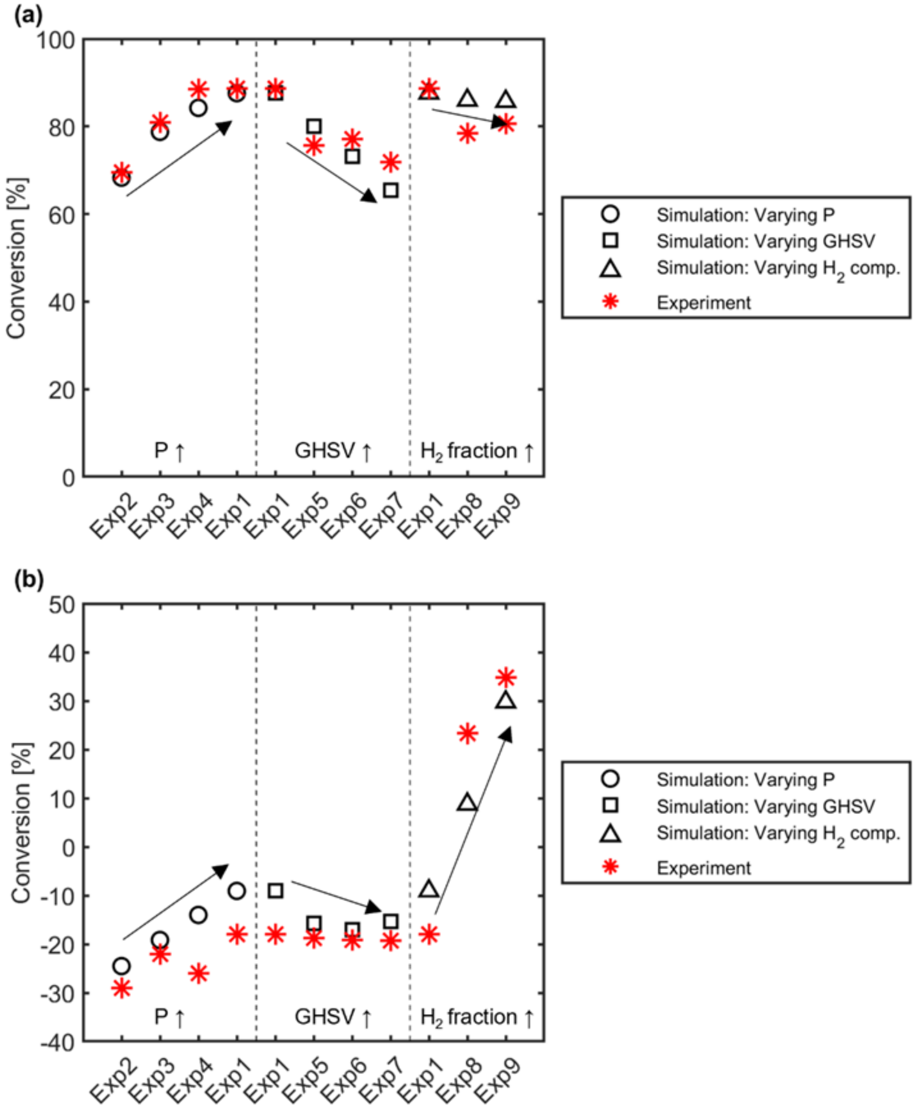

Figure 4 Comparison between simulation result and experimental data: CO and CO_2 conversion

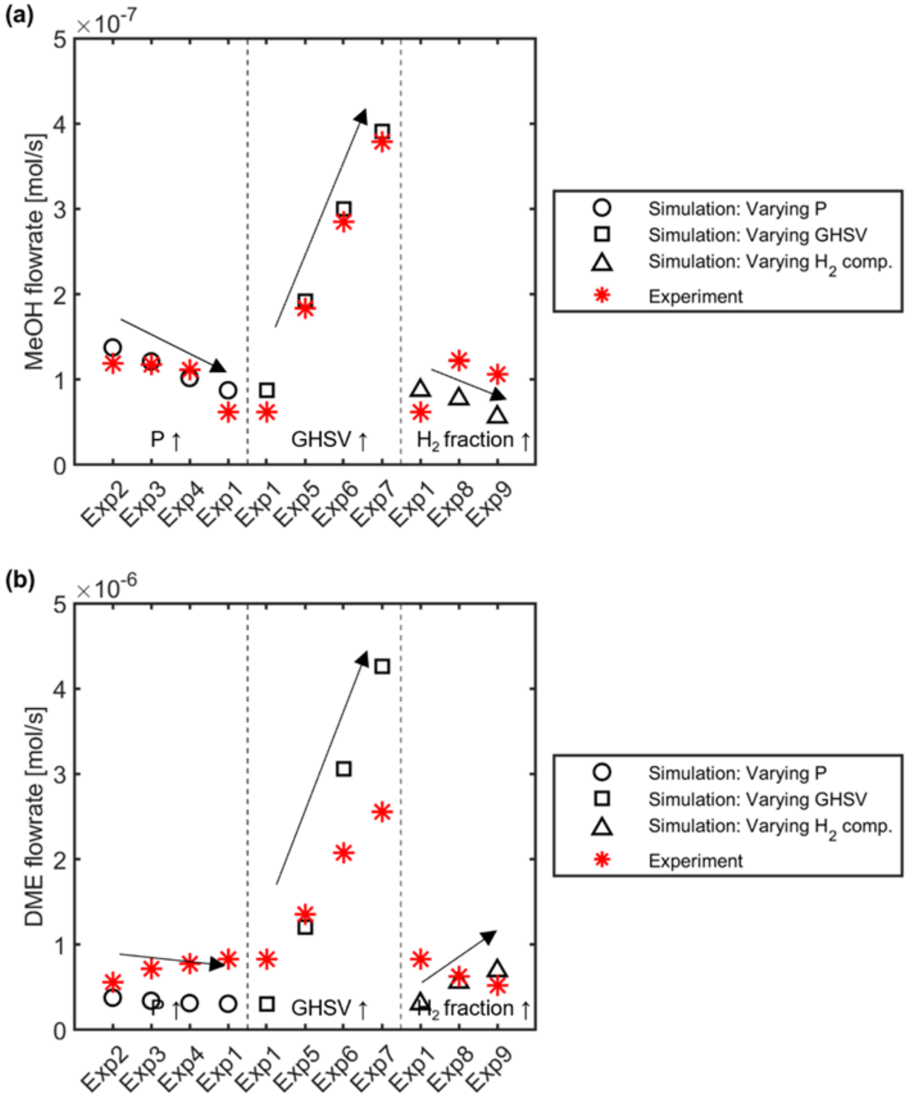

Figure 5 Comparison between simulation result and experimental data: MeOH and DME flowrate

3.3.1. Site Fractions

In the case of the CZA catalyst, the criterion of 10^{-8} was used to distinguish major and minor components, resulting in the fractions of CO*, CO_2*, H*, COOH*, and vacant sites to be the major components (Figure 6). Among the minor components, CH_2O* and HCOO** showed a relatively important proportion. Although HCOO** has been reported as a major component in the literature[11], [14], [37]–[39], COOH* was identified as the major surface component rather than HCOO** in this work. COOH* and HCOO** are involved in reactions 8, 9, 10, and reactions 14, 15, 22, respectively. In addition, the hydrogenation of HCOO** in reaction 15 is often considered a promising candidate for the rate-determining step (RDS)[14], [39]. This feature might be attributable that the reported works considered HCOO** as a monodentate component, while this study, as well as our previous work[1] assumed the bidentate adsorption of HCOO*. the result in this study does not consider HCOO** as a major component or a component related to the RDS. It is possible that both COOH* and HCOO** are considered as HCO_2, a simplified form[14]. It could be feasible that HCOO** shows low coverage, and COOH* shows high coverage in this study. Some studies did not consider HCOO* as an important intermediate. For example, Xu et al. [40] did not include HCOO* in their microkinetic model. Wu et al. [41] demonstrated that high HCOO* coverage could inhibit gas adsorption to vacant sites. Additionally, studies that suggested HCOO* is an essential intermediate included HCOOH, $HCOOCH_3$, and H_2COOCH_3[11], [42], which also showed differences from this study. The discussion of COOH* and HCOO** will be described further in the Reaction rates section based on the reaction rate results.

It is worth noting that CH_3OH* showed the lowest coverage, which is a significant difference from the results of the conventional MeOH synthesis. Low amount of MeOH on the catalytic surface indicates that the desorption of MeOH on CZA is significantly enhanced probably because the desorbed MeOH is instantly adsorbed onto the surface of FER in the shell of the hybrid catalyst.

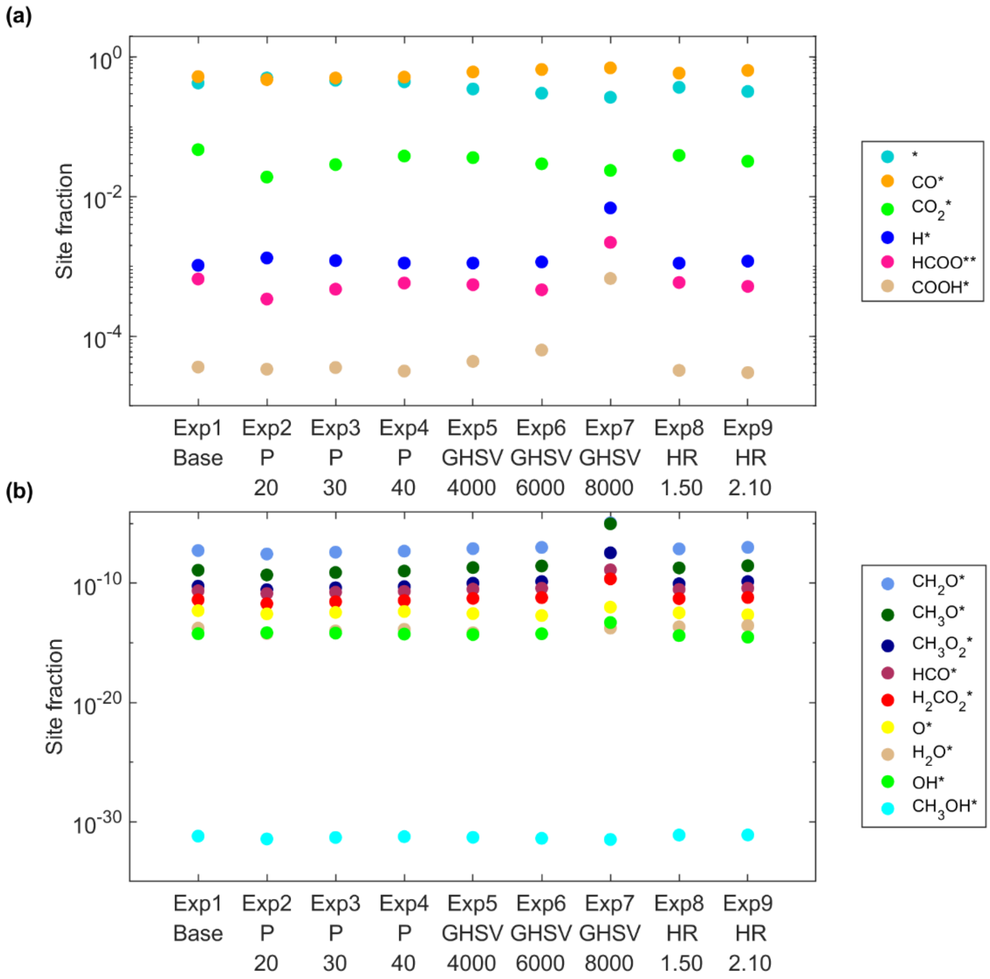

Figure 6 Simulation result: surface fractions over CZA. (a) major components, (b) minor components

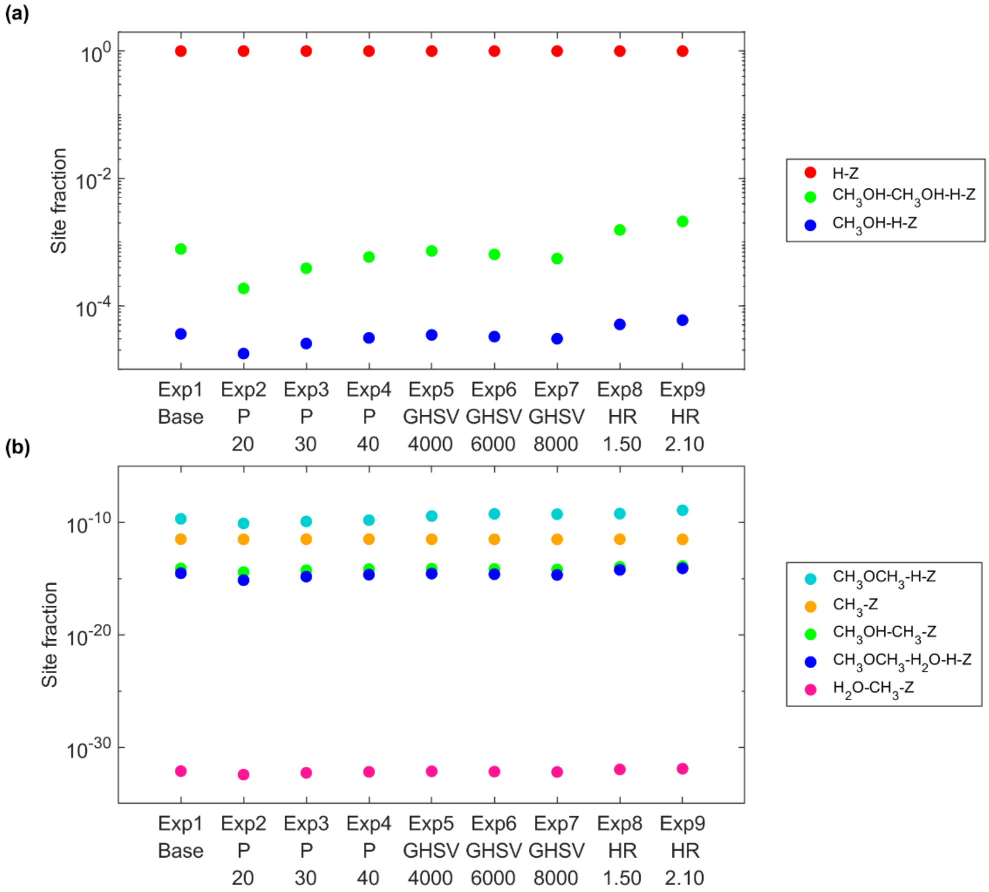

Figure 7 Simulation result: surface fractions over FER. (a) major components, (b) minor components

Criterion of the major and minor components in the FER catalyst was specified to be 10^{-10} (Figure 7). Among the major components, the dominance of vacant sites and CH_3OH-H-Z was similar to that of the previous FER catalyst model[3], whereas the dominance of CH_3OH-CH_3OH-H-Z, related to reaction 36, showed a clear difference from the previous research.[3] In the case of the minor components, the low fraction of CH_3OCH_3-H_2O-H-Z and H_2O-CH_3-Z was the same as in the previous research[3], whereas the proportion of CH_3-Z and CH_3OCH_3-H_2O-H-Z, which were considered major components in the previous research[3], was shown to be low in this work.

Notably, reaction 31, which was determined to be a rate-determining step for the dissociative path in the reported works[3], still showed an extremely small value for H_2O-CH_3-Z, while reaction 36, which was reported to be a rate-determining step for the associative path, showed a significant increase in the value of CH_3OH-CH_3OH-H-Z, resulting from the increased MeOH concentration in the CZA/FER hybrid catalyst.

3.3.2. Reaction Rates

The kinetic parameters and reaction rates of the microkinetic model were compared with those of our previous results.[1], [3] The reactions 9, 14, 19, and 28 were assumed to be at the partial equilibrium in the previous work[1] to reduce the number of the parameter set of the microkinetic model.[1] Meanwhile, the partial equilibrium assumption was not applied in this work. Additionally, the gas adsorption and desorption reactions (reactions 1-6) are not to be considered in equilibrium, which differs from our previous study.[3] The CO and CO_2 adsorption(reaction 1/reaction 2) equilibrium shifted towards the forward reaction compared to the previous research[3] results, while the H_2 and MeOH adsorption equilibrium shifted towards the reverse reaction. This phenomenon is likely due to the characteristics of the CZA catalyst located in the core of the core-shell structure. The gas-phase MeOH, $CH_3OH(g)$, is a product of the reaction occurring on the CZA catalyst and is generated by the desorption of CH_3OH^* (reaction 6) from the catalyst. Because the hybrid catalyst was constructed with a core-shell structure, the desorbed MeOH would be adsorbed to FER in the vicinity, resulting in the equilibrium($CH_3OH(g) + * \leftrightarrow CH_3OH^*$) moving to backward (more desorption).

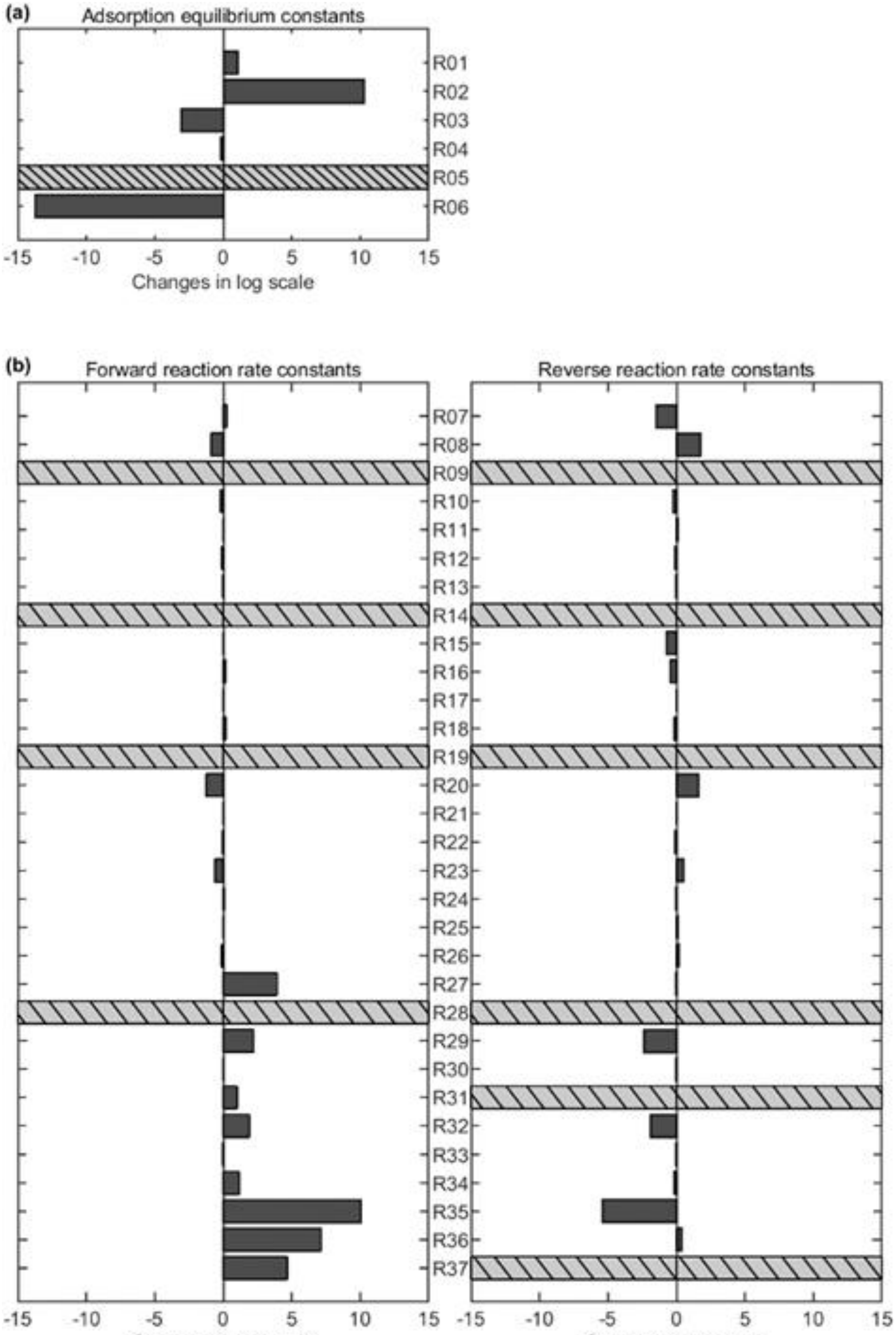

Figure 8 Change in reaction rate constant compared to previous research

In the case of the surface reactions, significant changes in reactions 7, 8, 20, 23, and 27 for CZA, and all surface reactions for FER were observed. The reactions which showed significant changes were noteworthy, particularly in reactions 7 (CO* + O* ↔ CO_2* + *) and 20 (CH_3O* + H* ↔ CH_3OH* + *), which were identified as rate-determining steps (RDS) in the previous work.[1] However, in this study, reactions 20 and 27 were found to be RDS, highlighting a key factor that distinguishes the reaction rate constants at the RDS between conventional and hybrid catalysts. Additionally, reaction 8 (CO* + OH* ↔ COOH* + *) is a reaction that includes COOH*, which is the dominant species in this study. The reaction 23 (HCO* + H ↔ CH_2O* + *) and 27 (CH_3O* + HCO* ↔ CH_3OH* + CO*) are related to the surface component HCO* and the reaction 26 (CH_3O* + CO* ↔ CH_2O* + HCO*), which was treated as the RDS in previous research.[1] In comparison to the previous research[1], reaction 7 (CO* + O* ↔ CO_2* + *) shifted towards the forward while reaction 8 (CO* + OH* ↔ COOH* + *) shifted towards the backward. This shift implies that the conversion of CO* to CO_2* over the hybrid catalyst increased in the direct path (reaction 7) and decreased in the indirect path (reactions 8-9) than previous work.[1]

In addition, the shift of reaction 20 (CH_3O* + H* ↔ CH_3OH* + *) towards the backward suggests that reaction 27 (CH_3O* + HCO* ↔ CH_3OH* + CO*) might provide an alternative pathway for producing MeOH* over the hybrid catalyst. Moreover, the changes in the parameters of reactions 20, 23, and 27 indicate that HCO* could become a key intermediate over the hybrid catalyst.

It is also necessary to examine the reaction rates to observe the reaction behavior. Figure 9 displays the forward, backward, and net reaction rates of each reaction calculated under the operating conditions of Exp1 (base case). In the net reaction rates chart on the right-hand side of Figure 9, the green color indicates a positive reaction rate, while the purple color indicates a negative reaction rate.

In Figure 9, the log-scaled reaction rates of the base case are presented. Apart from reaction 5 (CH_2O(g) + * ↔ CH_2O*), the forward and reverse reaction rates of reactions 1-6, 29, 32, and 35, which are gas adsorption/desorption reactions, are equal, indicating that adsorption and desorption reactions have reached equilibrium. For reaction 5, the gas component CH_2O(g) has a low concentration of approximately 10^{-18} mol/m^3, the reaction is rate-determining, although it is not found to have a significant effect on the overall system based on Campbell's degree of rate control analysis.[43]–[45] In the surface reactions over CZA, the reaction 7-9, 24 and 25 were particularly fast in the system. The reaction 8 was the main reaction of producing COOH*, which was one of the major surface component over CZA, and the fastest reaction in the system. As for the reaction that is commonly considered the rate-controlling step, reaction 20 (CH_3O^* + H* ↔ CH_3OH^* + *), it is also found to be a very slow reaction in this study, consistent with previous research[1] However, reaction 27 (CH_3O^* + HCO* ↔ CH_3OH^* + CO*) is found to have a higher forward rate compared to previous studies, as shown in Figure 8. This is believed to be due to the equilibrium of reaction 6 (CH_3OH(g) + * ↔ CH_3OH^*) shifting towards the desorption reaction (CH_3OH^* ↔ CH_3OH(g) + *) compared to previous studies, which helps to alleviate the bottleneck effect of the CH_3OH^* shortage. Before moving on to the reaction on the FER catalyst, we examined the reaction rates of reactions 9, 14, 19, and 28 that were excluded from the system in previous studies due to the assumption of partial equilibrium. As they all correspond to relatively fast reactions in the system, the assumption of partial equilibrium was appropriate. While reaction 9 (CO_2^* + H* ↔ COOH* + *) was in complete equilibrium in the previous study, the reverse reaction is higher than that of the forward reaction in this study. Furthermore, the forward reactions were favored in reaction 8 (CO* + OH* ↔ COOH* + *), which is the fastest reaction producing COOH*. This result is consistent with COOH* being identified as one of the major surface components.

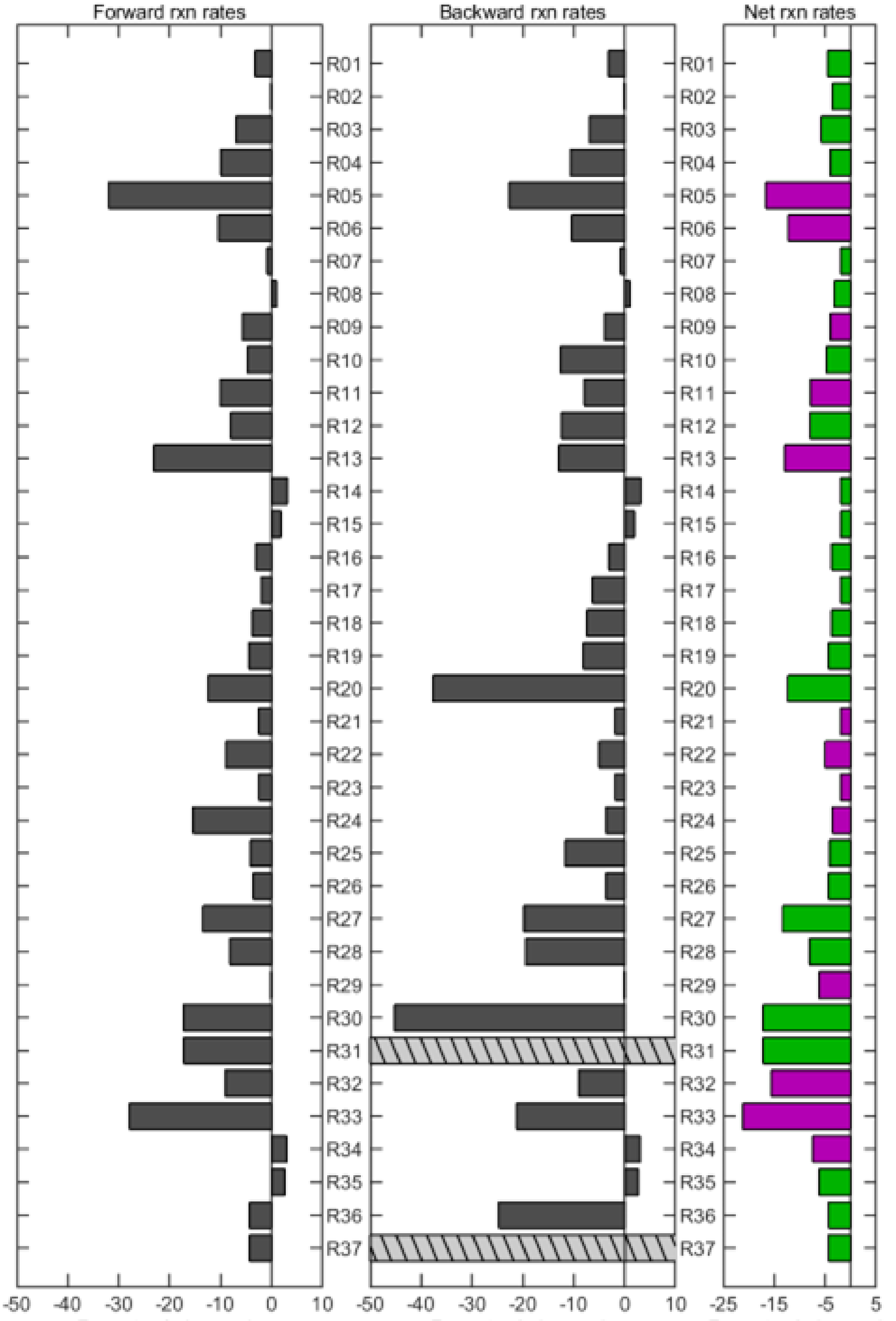

Figure 9 Forward, backward and net reaction rates using estimated parameter set in operating condition of Exp1: Base case (in log scale). The green color means the value in log is positive and the purple color means the value in log is negative.

As the result shown by figure 9, the main path of the CO conversion to CO_2 via HCO* and HCOO** is followed: forward reaction of reaction 21 (CO* + H* ↔ HCO* + *), reverse reaction of reaction 22 (HCO* + O* ↔ HCOO**) and reverse reaction of reaction 14 (HCOO** ↔ CO_2* + H*). Also, the CO conversion to MeOH via HCO*, CH_2O* and CH_3O* is followed: forward reaction of reaction 25 (CO* + H_2O* ↔ HCO* + OH*), reverse reaction of reaction 26 (CH_2O* + HCO* ↔ CH_3O* + CO*), forward reaction of reaction 20 (CH_3O* + H* ↔ CH_3OH* + *), forward reaction of reaction 27 (CH_3O* + HCO* ↔ CH_3OH* + CO*).

Moving on to the FER catalyst reactions (reactions 29-37), a brief review reveals that the reaction rates of MeOH adsorption reactions, specifically reactions 29, 32, and 35, increased in this system where MeOH diffusion was promoted. Moreover, it can be seen that the associative path, reactions 35-37, was accelerated more than the dissociative path, reactions 29-34.

To further investigate the effects of hydrogen concentration on CO_2 conversion, the reaction rates under high hydrogen composition in feed condition, Exp9, were compared with the base case, Exp1.

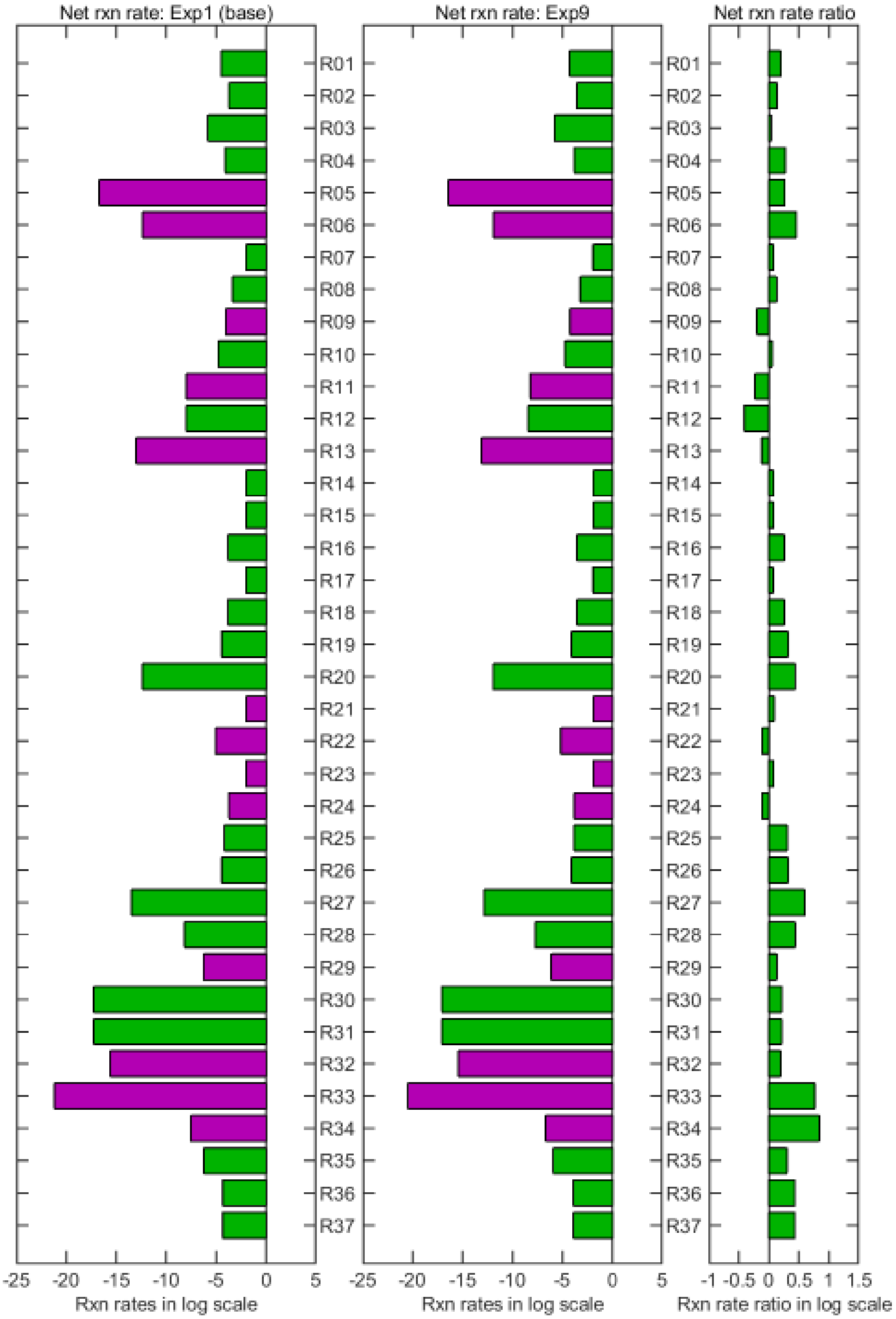

Figure 10 Ratio of the forward, backward and net reaction rates in the Exp9: High $\mathrm{H_{2}}$ composition in feed case to those in the base case (in log scale). The green color means the value in log is positive and the purple color means the value in log is

The reaction rates were investigated under high H_2 composition in feed conditions where CO_2 conversion occurs. Figure 10 shows the reaction rate difference in log scale between the Exp1 (base case) and Exp9. Except the reaction 21, signs of net reaction rates were same in high H_2 composition in feed conditions, Exp9, compared with the base case, Exp1. The reaction 20 and 27, the main reactions of CZA which produce CH_3OH^* increased in Exp9 than Exp1, which causes increasing MeOH production over CZA. As the production of MeOH over CZA increase, the MeOH adsorption to FER, the reaction rates of reaction 29, 32 and 35 also increased. This result in that evenif the MeOH production over CZA increased in Exp9 than Exp1, the adsortion reactions, reaction 6, 29, 32 and 35 also getting faster so that the overall MeOH production rate decreased, which was shown in Figure 9. The reaction rate of reactions 8 ($CO^* + OH^* \leftrightarrow COOH^* + *$) slightly increased, as contrast with the reaction rates of reaction 9 ($CO_2^* + H^* \leftrightarrow COOH^* + *$) decreased, indicating the equilibrium of reaction 9, which has H^* as a reactant, moved to forward in increase of H_2 composition in feed (Exp9). The result for the reaction 21 shows interesting point that the sign of net reactions changed and is a relatively fast reaction in the system and involved in the main path of CO conversion to CO_2 and MeOH. As the figure of site fraction over CZA in figure 6, the site fraction of CO^* increased and the vacant site fraction decreased in Exp9 than Exp1. The shift to net reverse in reaction 21 ($CO^* + H^* \leftrightarrow HCO^* + *$) can explain the changes of site fraction of CO^* and the vacant in Exp9. Also, the CO_2 consumption in high H_2 composition condition, in Exp8-9, can be explained with the changes in reaction 21. The main path of CO conversion is forward reaction of reaction 21, backward reaction of reaction 22 and backward reaction of reaction 14 shows getting slower with Exp9 condition in Figure 10. The reactions related with producing CH_3OH^* are reaction 19-20 and 26-28 and those shows getting faster with Exp9 condition in Figure 10. The increase of CH_3OH^* results in a shift in the equilibrium point of reaction 6 towards the desorption reaction and accelerated the FER catalytic reaction, particularly the associative path, which appears to be a MeOH diffusion-controlled system based on the partial pressure of MeOH.[7] The surface component $HCOO^{**}$ is related with reaction 14, 15 and 22, which decreased in Exp9, in high H_2 composition in feed condition. The studies suggesting $HCOO^*$[11], [14] is important or is related with the RDS, was results from relatively low H_2 composition in feed condition. Moreover, Grabow et al.[11] showed the calculation result that the site fraction of $HCOO^*$ increases in low H_2, and high CO_2 composition in feed condition.

It should be noted that the tendency of model in predicting DME production rates didnt't match with experimental values under increasing the H_2 composition in feed condition, Exp1 and 8-9. It would be due to limitations in the model's ability to capture the complexities of the catalytic system. It might exaggerate the effect of the increase in reaction rates of reactions 19 and 20 on CH_3OH^* production and the consequent promotion of the adsorption reactions for MeOH over FER (reactions 29, 32, and 35) in the modeling, or it could also be resulted from experimental error.

3.3.3. Case Study: Converting CO2 into MeOH and DME

Examining the experimental results shows that the CO_2 conversion was represented in cases with high H_2 composition in the feed. In most cases, negative CO_2 conversion was shown, meaning the generation of CO_2, but in experimental runs 8 and 9, with two high H_2 composition in feed conditions from all nine experimental runs, positive CO_2 conversion was shown, meaning the consumption and conversion of CO_2. Based on these experimental results, a case study was performed to find the region that represents positive CO_2 conversion through reproducing the results in a model. The calculation of a total of 27,000 points for case studies was performed based on 30 points interpolation for each variable, while the ratio of CO and CO_2 in the feed was fixed within the experimental conditions of temperature 250 ℃, pressure 20-50 bar, GHSV 2000-8000 L/(kg_{cat} h), and $H_2/(2CO+3CO_2)$ value range of 0.96-2.1.

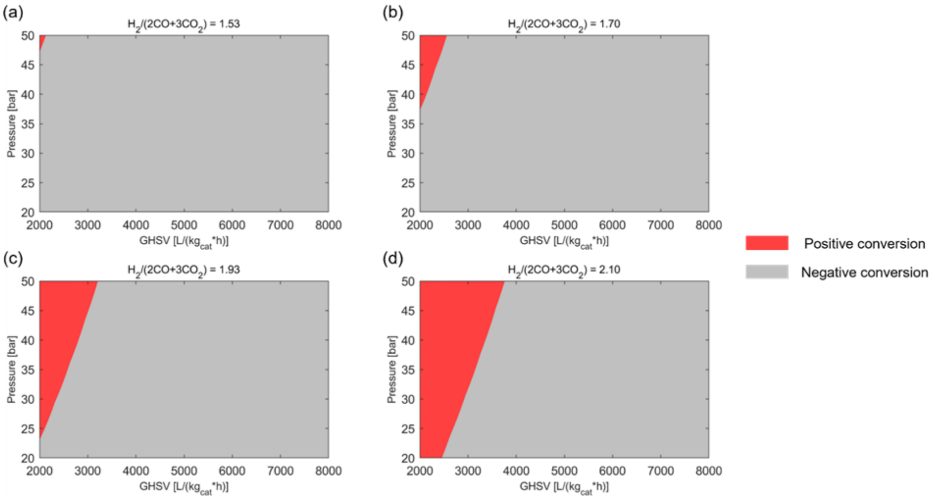

Figure 11 Case study result: the colored area represents whether the CO_2 conversion is positive or negative. The area covered by red color is the region where CO_2 conversion is positive, and the area covered by gray color is the region where CO_2 conversion is negative.

According to the case study results in Figure 11, CO_2 consumption occurred at lower pressures and higher GHSV values as the $H_2/(2CO+3CO_2)$ value increased, but when the GHSV value exceeded 4000, CO_2 was produced at all the pressure and GHSV. Since high GHSV values are required for high productivity, it appears that there is a trade-off between CO_2 conversion and productivity. To convert CO_2 at high GHSV, higher $H_2/(2CO+3CO_2)$ values and higher pressure are required, which are not recommended operating conditions.

Chapter 4. Lumped Kinetic Modeling of Catalytic Deactivation of Aromatization from Ethane and Propane over Ga/ZSM-5

4.1. Background

Since the beginning of the 21st century, the worldwide energy source is on a continuous shift towards unconventional sources, which is further accelerated by the dramatic increase in natural gas production.[46], [47] Among the various valorization techniques of such natural gas supply, direct non-oxidative aromatization to light aromatics such as BTX (benzene, toluene, and xylene) is considered as a potential alternative to conventional BTX production processes. [40], [48]–[50] Indeed, propane aromatization is a relevant reaction that has attracted great attention from both the academic and industrial society, due to the high reactivity of propane that makes the reaction relatively feasible, compared to other hydrocarbon components of natural gas (methane or ethane). [51], [52]

Due to their unique characteristics including porosity and acidity, zeolites have been widely applied in the field of alkane aromatization. Especially, the 10 membered-ring structure of MFI zeolites is known to promote the selective production of light aromatics, making ZSM-5 the most popular catalyst for the reaction. [53], [54] It has also been well established that the addition of Ga as an active metal further enhances the catalytic performance, and still to this date, Ga/ZSM-5 remains as the state-of-the-art catalyst for propane aromatization [55]–[57]. Although the exact working mechanism of the catalyst remains rather controversial, it is generally believed that the reaction progresses in a bi-functional manner: propane is initially activated by Ga sites to generate olefinic intermediates, which then are oligomerized and cyclized to aromatics by Brønsted acid sites of the zeolite [58], [59]. Despite the abundance of works devoted to improve the performance of Ga/ZSM-5, however, its rapid catalytic deactivation due to intensive coke formation still remains as the fundamental hurdle to rigorous industrialization of the process [60], [61]. Therefore, to understand the Ga/ZSM-5 system from an industrial process perspective, it is important to accurately simulate deactivation in the modeling.

Deactivation of catalytic reactions is a major challenge that limits the efficiency and longevity of industrial processes. Catalyst deactivation, a gradual decay of catalytic activity and selectivity, is an inevitable process that can occur through several mechanisms, including poisoning, sintering, thermal degradation, and coking. An understanding of these mechanisms, their implications, and methods to mitigate them is central to maintaining the efficiency and sustainability of catalytic processes.

Poisoning is often due to the strong chemisorption of specific molecules onto the active sites, while sintering and thermal degradation occur primarily due to the high operating temperatures that may lead to changes in the catalyst's physical structure. Nevertheless, coking is one of the most common causes of catalyst deactivation, particularly in processes involving hydrocarbons.[62]

Coking is the formation of carbonaceous deposits on the catalyst surface during the reaction process. Hydrocarbon feedstocks, under certain conditions, can decompose or polymerize, leading to the formation of these coke deposits. As coke accumulates, it begins to obstruct active sites on the catalyst, which directly inhibits the catalyst's performance. The detrimental impact of coking is two-fold: it not only blocks the catalyst's active sites but also influences the diffusion of reactants and products, hindering the overall reaction rate. The resulting decrease in catalytic activity can be dramatic, necessitating either the replacement of the catalyst or a regeneration process to burn off the coke deposits.

Understanding the mechanism and kinetics of coking is crucial for the development of more resilient catalysts and more efficient processes. Strategies to mitigate coking include the design of catalysts that are less prone to coke formation, optimization of reaction conditions to minimize coke formation, and incorporation of efficient catalyst regeneration steps into the process.

In the context of sustainable chemical processing, addressing the challenge of catalyst deactivation, especially through coking, is a significant area of research. The development of strategies to minimize catalyst deactivation will not only improve the economic viability of processes but will also contribute to the broader goal of sustainable and efficient chemical production.

4.2. Lumped Kinetic Modeling and Reaction Mechanism

The Ga/ZSM-5 catalyst is known for its bifunctional nature, which means it has two distinct active sites that contribute to the overall reaction mechanism. These are the Ga-sites (Lewis acid sites, LAS) and H-sites (Brønsted acid sites, BAS).

The Ga-sites are Lewis acid sites, which are characterized by an electron-deficient center that can accept an electron pair. These sites are primarily responsible for the adsorption and dehydrogenation reactions. Adsorption is the process where molecules adhere to the surface of the catalyst. Dehydrogenation is a chemical reaction that involves the removal of hydrogen from a molecule. In the context of light alkane conversion over Ga/ZSM-5, the Ga-sites adsorb the alkane and facilitate its dehydrogenation, forming an alkene and releasing hydrogen. This alkene can then participate in further reactions, such as oligomerization at the H-sites.

On the other hand, the H-sites are Brønsted acid sites, which are characterized by a proton that can be donated during the reaction. These sites are primarily responsible for the oligomerization reactions. Oligomerization is a process where smaller molecules (like ethane and propane) combine to form larger hydrocarbon chains. This is a key step in the conversion of light alkanes to aromatics. The H-sites facilitate the protonation of the alkane, leading to the formation of a carbocation. This carbocation can then react with other alkanes to form larger hydrocarbon species.

In the aromatization of ethane and propane, which is the subject of this study, adsorbed intermediates of C_2H_6* and C_3H_8* are formed through the adsorption equilibrium of ethane and propane at the Lewis Acid Site (LAS), the Ga-site. These intermediates are designed to have three possible reactions: dehydrogenation, cracking, or coking. Propane is known to have high reactivity over ZSM-5 catalyst [63], [64], so it is reasonable to assume that the cracked adsorbed intermediates are more likely to undergo additional reactions rather than being immediately desorbed. The experimental values in the system covered in this study will be reviewed and further explained below. The catalyst showed the highest activity at 650 degrees Celsius in the Ga/ZSM-5 ethane and propane aromatization experiments conducted at three temperatures: 550, 600, and 650 degrees Celsius. Therefore, we will focus on the experimental values at 650 degrees Celsius and describe the reaction mechanism set in this study.

Experimental runs 1-3 were conducted at 650 degrees Celsius, and the ethane, propane conversion, and benzene, toluene, xylene, and naphthalene (BTXN) yield in these experiments are shown in figures 13-15. The yield of ethylene and propylene in each run is summarized in figures 16-18. Experimental runs 1-2 are characterized by a feed composed only of nitrogen and propane at 650 degrees Celsius. Looking at figures 16-18, which show the yield of ethylene and propylene in these runs, we can confirm that not only propylene but also ethylene is produced through the reaction conducted with this propane feed, and our research team judged that propane was cracked after being adsorbed on Ga/ZSM-5 to form ethylene.

The adsorption reaction on Ga/ZSM-5 is known to occur at the LAS, the Ga-site [48], [65], [66]. Therefore, our research team checked the conversion of experimental results related to the adsorption reaction to set the reaction mechanism at the LAS. Looking at the ethane, propane conversion in figure 15 of experimental run 3, which conducted the experiment with ethane, propane co-feed, we can confirm that although the ethane conversion forms a significantly lower value compared to the propane conversion, it does not show a negative conversion. Based on this, our research team was able to confirm that ethane is not favorable enough to compete in Ga/ZSM-5 adsorption compared to propane, and it can be assumed that the adsorbed-propane intermediate, C_3H_8*, is largely dehydrogenated to form propylene or cracked to form the adsorbed-ethane intermediate, C_2H_6*, and that the adsorbed-ethane C_2H_6* largely undergoes dehydrogenation to form ethylene. Considering that ethylene is produced from a feed containing only propane, it is natural to assume that C_3H_8* is cracked to form C_2H_6*, and when it is consistently assumed that dehydrogenation and cracking, coking occur in this case, if the dehydrogenation and cracking ratio is low, C_2H_6* is not favorable in Ga/ZSM-5 adsorption, so it is easy to show a negative value in ethane conversion, but considering that it did not show a negative value in this experiment, it can be seen that C_2H_6* undergoes additional reactions. In addition, looking at the experimental values, it can be assumed that a certain part of the cracking reaction from C_2H_6* to CH_4* occurs as the methane yield is lower than the propane yield.

$$\theta_{C_2H_6*} = \frac{K_{C_2}P_{C_2}}{1 + K_{C_2}P_{C_2} + K_{C_3}P_{C_3}}$$

$$\theta_{C_3H_8*} = \frac{K_{C_3}P_{C_3}}{1 + K_{C_2}P_{C_2} + K_{C_3}P_{C_3}}$$

$$\gamma_{dehydro,C_2} + \gamma_{crack,C_2} + \gamma_{coke,C_2} = 1$$

$$\gamma_{dehydro,C_3} + \gamma_{crack,C_3} + \gamma_{coke,C_3} = 1$$

In the context of coke formation, it was not observed that the case of propane with ethane co-feed led to more rapid deactivation through the formation of more coke compared to the propane feed. An additional point worth examining through the analysis of experimental values is that different deactivation curves are formed for conversion and yield. As seen in Figures 13-15, although ethane and propane conversion become deactivated as the reaction progresses, they do not become fully deactivated and conversion does not drop to zero. However, the yield of BTXN approaches zero as it becomes fully deactivated as the reaction progresses. In addition to this, our research team, noting that the gas adsorption reaction involved in conversion occurs at the Ga-site, the LAS in Ga/ZSM-5, and the oligomerization and cyclization reaction involved in BTXN yield occurs at the H-site, the BAS, assumed that deactivation due to coking proceeds independently at the LAS and BAS based on the amount of coke deposited and accumulated in our model development.

$$Deactiavation_{de\hbar ydro(LAS)}\left(\theta_{coke,LAS}\right) = 1 - \theta_{coke,LAS}$$

$$\theta_{coke,LAS} = \frac{\dot{y}_{coke,LAS}}{\dot{y}_{coke\ max,LAS}} * \frac{1}{\theta_{C_2} + \theta_{C_3}}$$

$$Deactiavation_{de\hbar ydro(BAS)}\left(\theta_{coke,BAS}\right) = 1 - \theta_{coke,BAS}$$

$$\theta_{coke,BAS} = \frac{\dot{y}_{coke,BAS} + \alpha * \dot{y}_{coke,LAS}}{\dot{y}_{coke\ max,BAS}} * \frac{1}{\theta_{C_2} + \theta_{C_3}}$$

Figure 19-30 shows the ethane and propane conversion, BTXN yield, and ethylene and propylene yield in Experimental runs 4-9. By looking at Figure 19-21, which shows the ethane and propane conversion and BTXN yield in Experimental run 4-6 at 600 degrees, and Figure 25-27, which shows the ethane and propane conversion and BTXN yield in Experimental run 7-9 at 550 degrees, we can confirm that the tendency of deactivation significantly decreases as the reaction temperature decreases. Through these results, our research team was able to reconfirm the existing research results[67] that deactivation occurs as the reaction progresses, that is, due to the deposit of coked, a reaction by-product. Therefore, we proceeded with modeling under the assumption that deactivation occurs due to the deposit of Coke. According to M. Guisnet[62], the H/C ratio of accumulated cokes in the catalyst decreases as the reaction progresses. Based on this, our research team believed that the coke produced by the adsorption reaction at the Ga-site, the LAS, is major at the beginning of the reaction, but as the reaction progresses, the aromatic coke produced as a by-product of oligomerization at the H-site, the BAS, becomes major. In addition, according to [62], this aromatic coke is further reacted in the process of forming polycyclic aromatic hydrocarbons from the oligomerization & cyclization process, passing through naphthalene. The fact that the carbon yield of naphthalene in our research team's experimental results shows a value that is not negligible compared to BTX, and that it is advantageous to introduce from BTX to aromatic coke via naphthalene in reproducing the experimental phenomenon where the peak of BTX yield appears, are two reasons why the introduction of this reaction mechanism is considered valid.

Finally, I will describe the reactions occurring at the Brønsted acid sites (BAS), known for oligomerization and cyclization. The reactions at the BAS begin with the formation of protonated carbocations due to the protonation of light olefins arranged within the ring structure of the zeolite at the H-site [62], [65], [68]. These protonated carbocations propagate to proceed with oligomerization. Most of the previous studies have viewed the diverse distribution phenomena of these carbocations as a hydrocarbon pool rather than simulating all sizes of protonated carbocations. Since various reactions can occur in this hydrocarbon pool, the reactions at the BAS were handled using a lumped kinetic mechanism rather than constructing a system with elementary reactions. Our research team also used a lumped kinetic based on the hydrocarbon pool for the reactions at the BAS, following the same principle as previous studies. However, a few previous studies[62], [65], [68], considered C4 diene as an important intermediate, but in our GC experimental results, the C4+ yield did not show a significant value, making it impossible to verify the C4 diene. Therefore, we excluded the unverifiable C4 diene from the reaction species and proceeded with modeling. Hence, in our team, only ethylene and propylene were set as reaction products in oligomerization, and modeling was conducted.

In summary, the H-sites and Ga-sites over Ga/ZSM-5 play complementary roles in the conversion of light alkanes to aromatics. The Ga-sites facilitate the initial adsorption and dehydrogenation of the alkane, forming an alkene. This alkene can then react at the H-sites, undergoing oligomerization to form larger hydrocarbon species. These larger species can then undergo further reactions, such as cyclization and dehydrogenation, to form aromatic compounds. The overall reaction mechanism is shown in below Table 6.

Table 6 Overall reaction mechanism of ethane/propane aromatization over Ga/ZSM-5

No.	Reaction	Site fraction	Reaction Type
R1	$C_2H_6 + * \leftrightarrow C_2H_6*$	$\theta_{C_2H_6*} = \frac{K_{C_2}P_{C_2}}{1 + K_{C_2}P_{C_2} + K_{C_3}P_{C_3}}$	Adsorption Equilibrium (LAS)
R2	$C_3H_8 + * \leftrightarrow C_3H_8*$	$\theta_{C_3H_8*} = \frac{K_{C_3}P_{C_3}}{1 + K_{C_2}P_{C_2} + K_{C_3}P_{C_3}}$	
No.	Reaction	Reaction rate	
R3	$C_2H_6* \rightarrow C_2H_4* + H_2$	$k_3\gamma_{C_2Dehydro}\theta_{C_2H_6*} * f_{Deact,LAS}$	Irreversible Reaction (LAS)
R4	$C_2H_6* + H_2 \rightarrow CH_4* + CH_4$	$k_4\gamma_{C_2Crack}\theta_{C_2H_6*} * f_{Deact,LAS}$	
R5	$C_2H_6* \rightarrow$ Coke	$k_5\gamma_{C_2Coke}\theta_{C_2H_6*} * f_{Deact,LAS}$	
R6	$C_3H_8* \rightarrow C_3H_6* + H_2$	$k_6\gamma_{C_3Dehydro}\theta_{C_3H_8*} * f_{Deact,LAS}$	
R7	$C_3H_8* + H2 \rightarrow C_2H_6* + CH_4$	$k_7\gamma_{C_3Crack}\theta_{C_3H_8*} * f_{Deact,LAS}$	
R8	$C_3H_8* \rightarrow$ Coke	$k_8\gamma_{C_3Coke}\theta_{C_3H_8*} * f_{Deact,LAS}$	
R9	$3C_2H_4 \rightarrow$ Benzene + 3H2	$k_9P_{C_2H_4} * f_{Deact,BAS}$	Irreversible Reaction (BAS)
R10	$2C_3H_6 \rightarrow$ Benzene + 3H2	$k_{10}P_{\mathrm{C_3H_6}} * f_{Deact,BAS}$	
R11	$2C_2H_4 + C_3H_6 \rightarrow$ Toluene + $2H_2$	$k_{11}P_{\mathrm{C_2H_4}}P_{\mathrm{C_3H_6}} * f_{Deact,BAS}$	
R12	$C_2H_4 + 2C_3H_6 \rightarrow$ Xylene + $3H_2$	$k_{12}P_{\mathrm{C_2H_4}}P_{\mathrm{C_3H_6}} * f_{Deact,BAS}$	
R13	Benzene + $2C_2H_4 \rightarrow$ Naphthalene + $3H_2$	$k_{13}P_{Benzene}P_{\mathrm{C_2H_4}} * f_{Deact,BAS}$	
R14	Toluene + $C_3H_6 \rightarrow$ Naphthalene + $3H_2$	$k_{14}P_{Toluene}P_{\mathrm{C_3H_6}} * f_{Deact,BAS}$	
R15	Xylene + $C_2H_4 \rightarrow$ Naphthalene + $3H_2$	$k_{15}P_{Xylene}P_{\mathrm{C_2H_4}} * f_{Deact,BAS}$	
R16	Naphthalene $\rightarrow$ Coke	$k_{16}P_{Naphthalene} * f_{Deact,BAS}$	

This study is significant in that it conducted long-term dynamic modeling by setting the coke site fraction based on the Langmuir adsorbate equation as the main variable for deactivation, by comprehensively reviewing the lab-scale experimental results of ethylene and propane aromatization in Ga/ZSM-5 and the previous research results of other researchers, and by separating the deactivation at the Lewis acid sites (LAS) and BAS. Most of the previous studies were conducted with a time on stream (TOS) of less than 30 minutes, and even in studies like that of L. H. Nguyen et al.[69], which considered a relatively long TOS, they only considered up to 3 hours. Therefore, the long-term dynamic catalytic deactivation modeling up to a maximum of 10 hours handled in this study is meaningful. Lastly, it was confirmed that the simulation result of this study, which applied the deactivation model, could reproduce the experimental result.

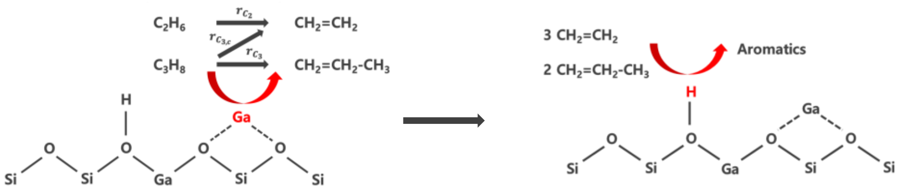

Figure 12 ethane and propane aromatization over Ga/ZSM-5: reaction scheme over Ga-site(LAS) and H-site(BAS)

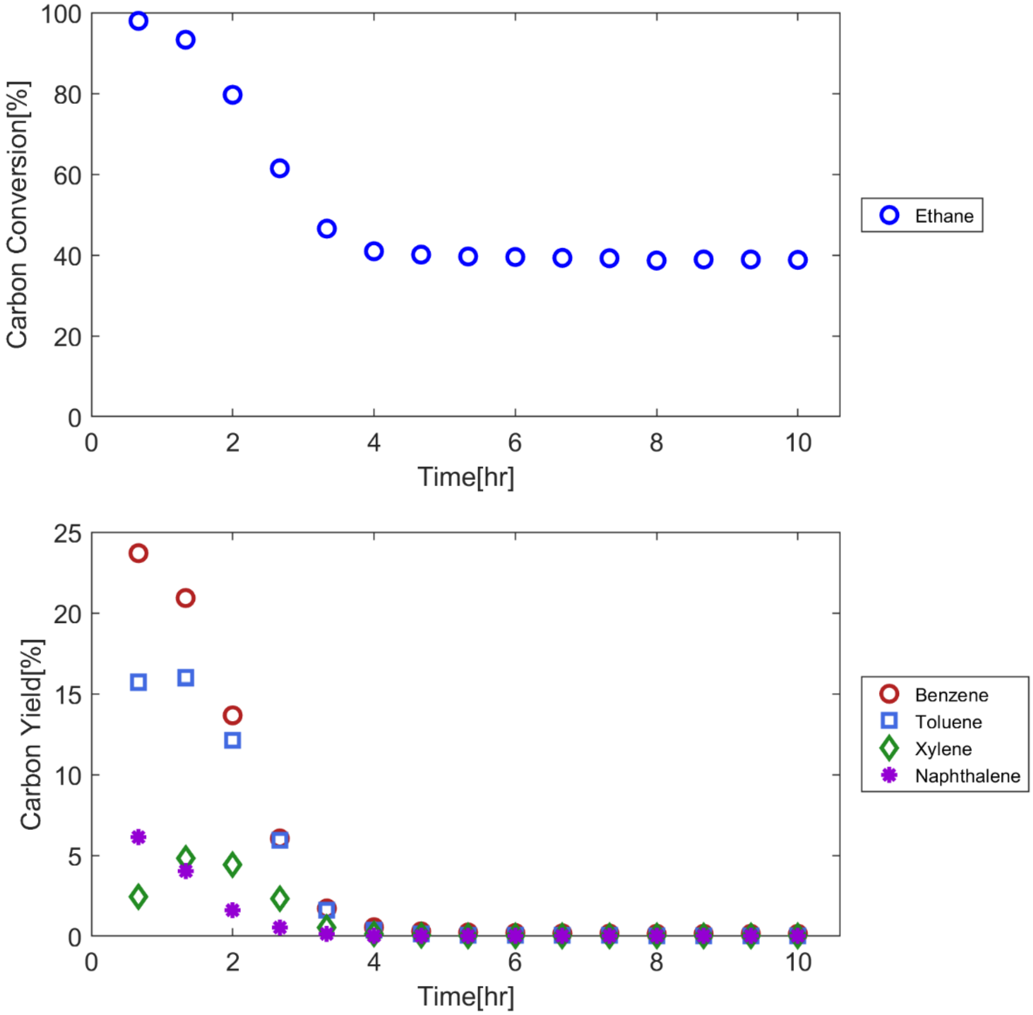

Figure 13 Experimental result of reactant conversion and product yield: N_2(6), C_2(0), C_3(6) at 650℃.

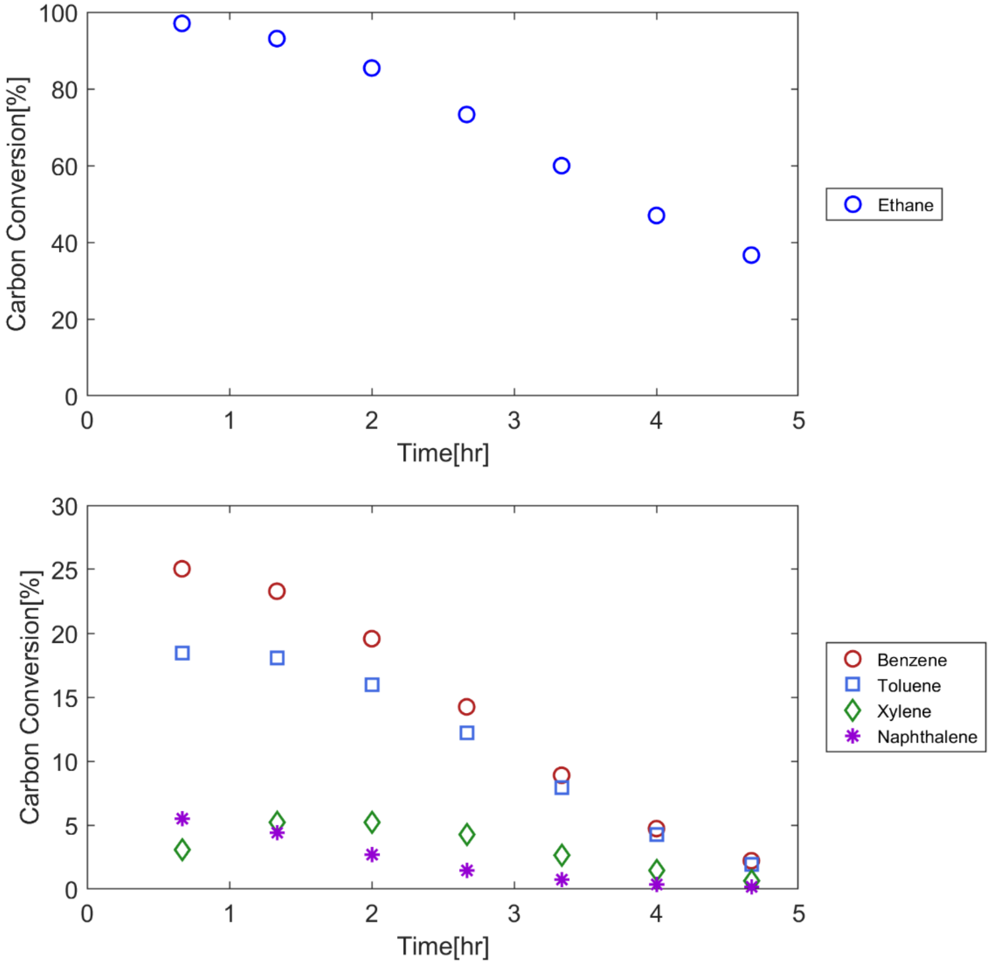

Figure 14 Experimental result of reactant conversion and product yield: N_2(8), C_2(0), C_3(4) at 650°C.

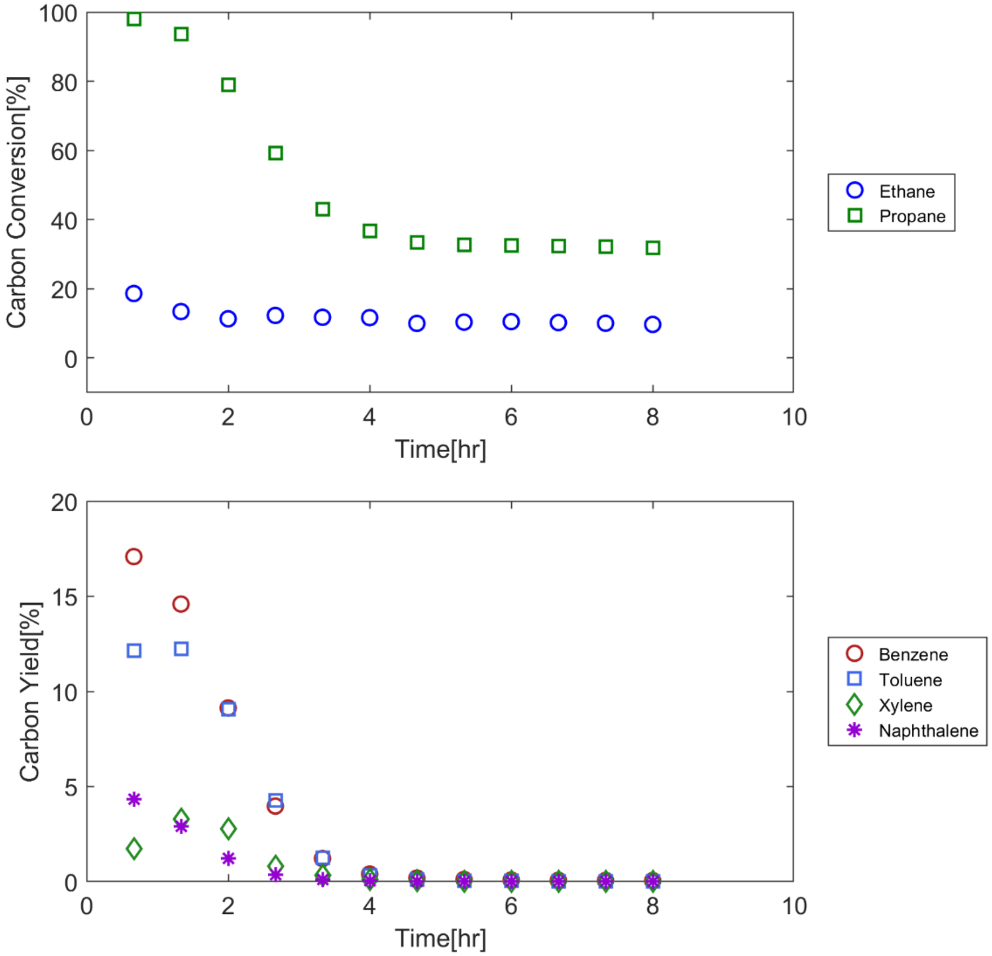

Figure 15 Experimental result of reactant conversion and product yield: N_2(6), C_2(3), C_3(3) at 650°C.

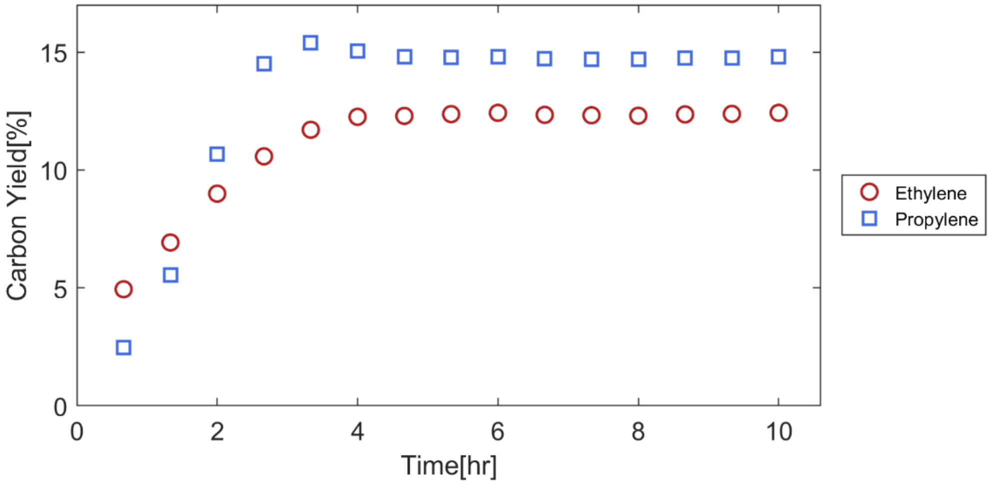

Figure 16 Experimental result of ethylene and propylene yield: N_2(6), C_2(0), C_3(6) at 650℃.

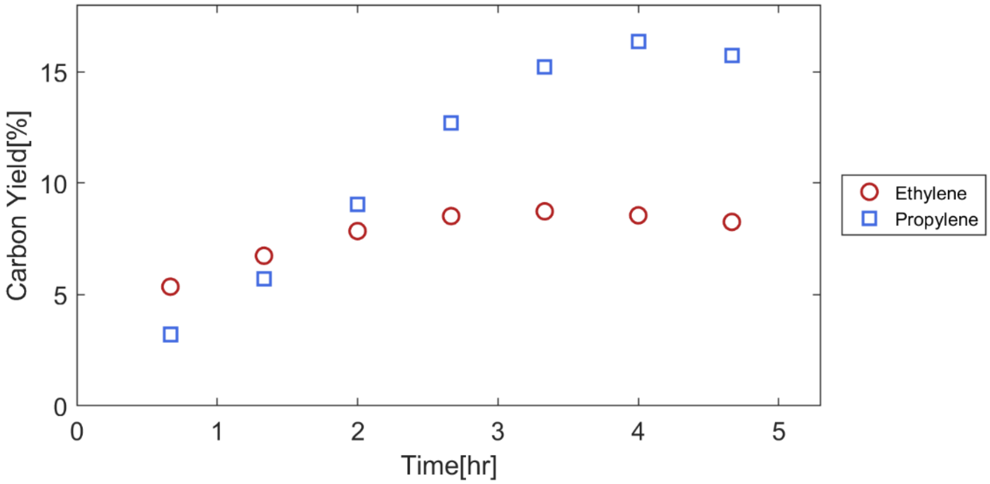

Figure 17 Experimental result of ethylene and propylene yield: N_2(8), C_2(0), C_3(4) at 650℃.

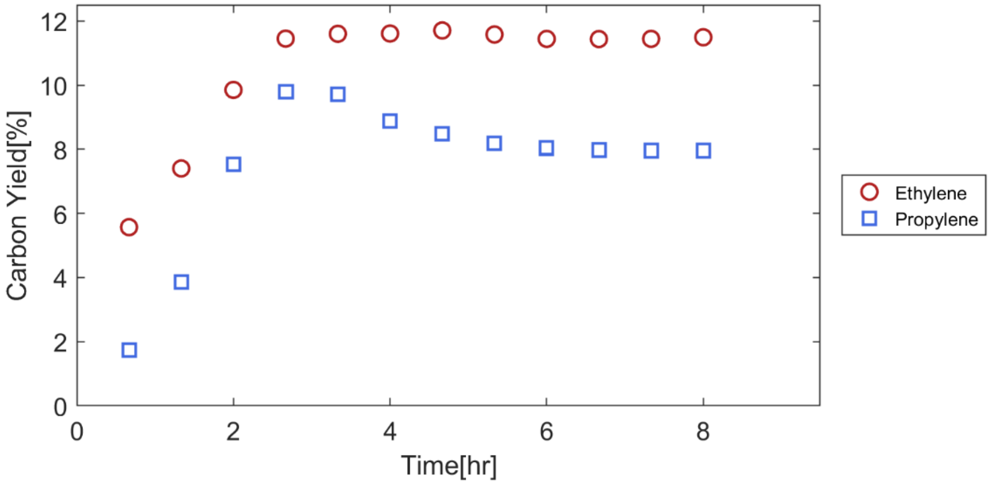

Figure 18 Experimental result of ethylene and propylene yield: N_2(6), C_2(3), C_3(3) at 650℃.

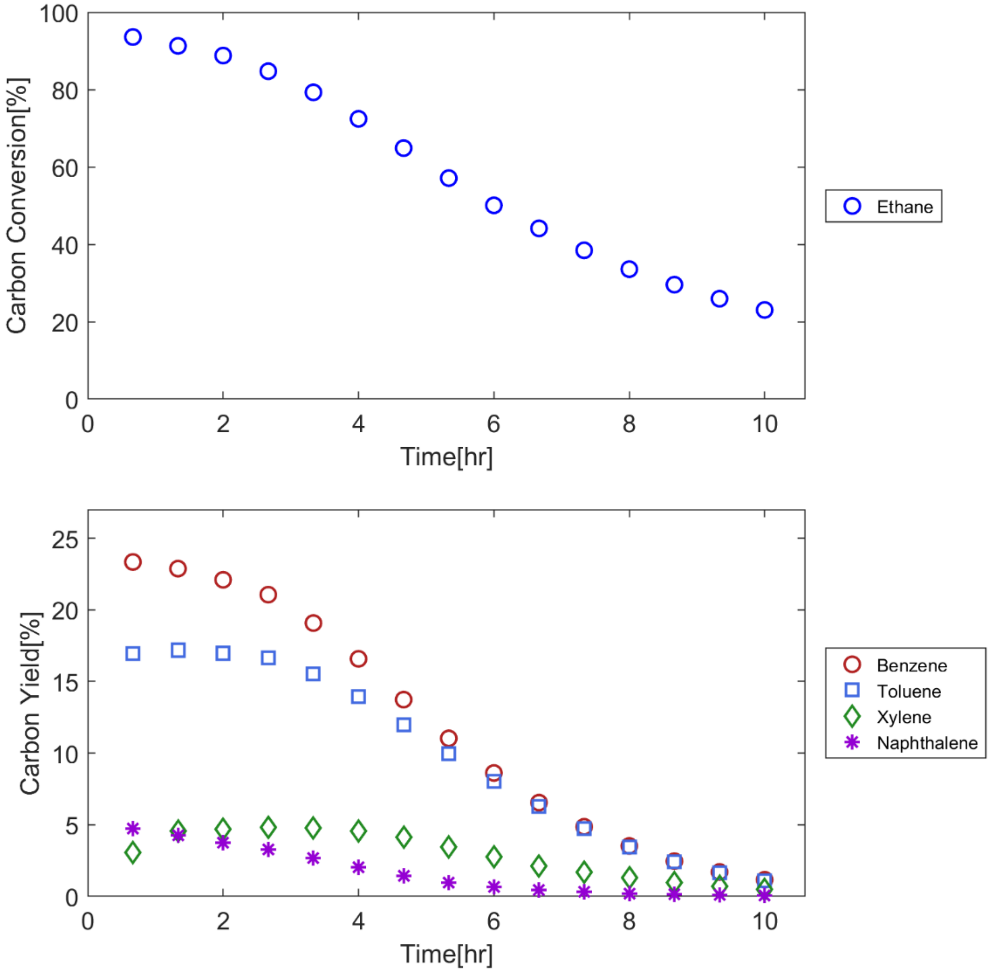

Figure 19 Experimental result of reactant conversion and product yield: N_2(6), C_2(0), C_3(6) at 600°C.

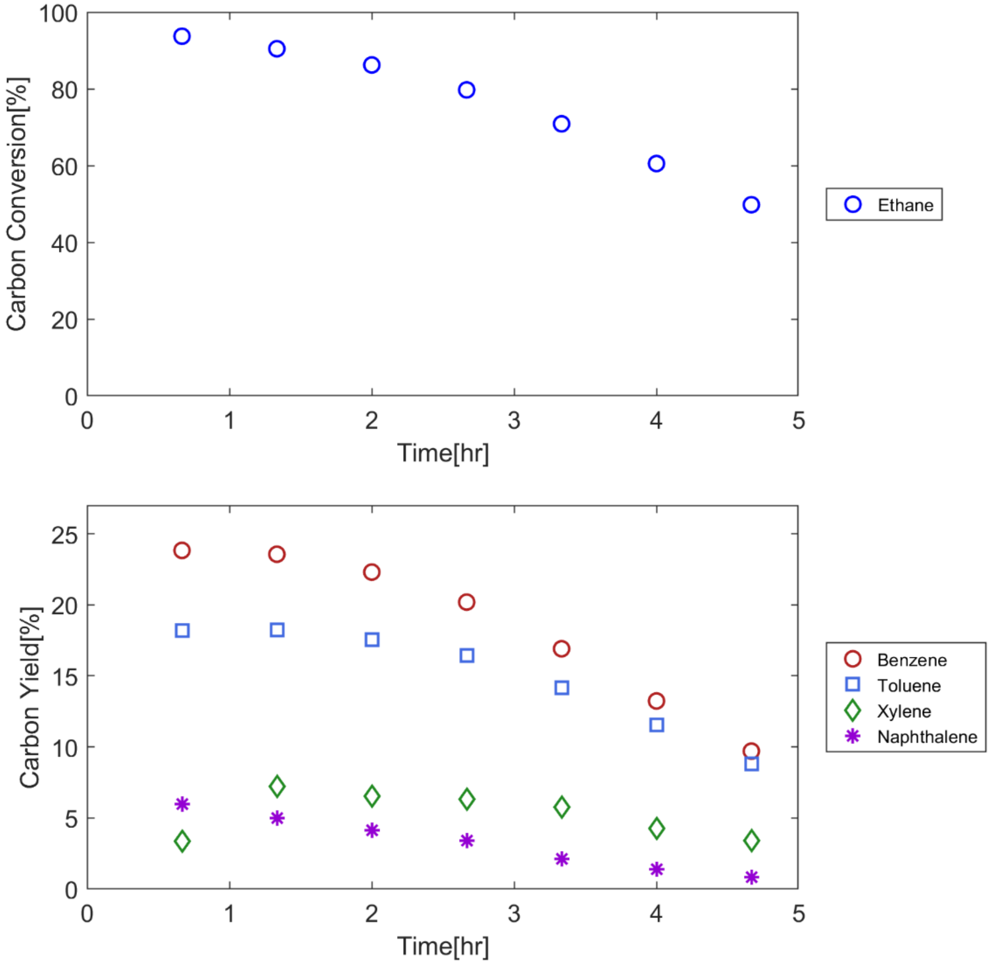

Figure 20 Experimental result of reactant conversion and product yield: N_2(8), C_2(0), C_3(4) at 600°C.

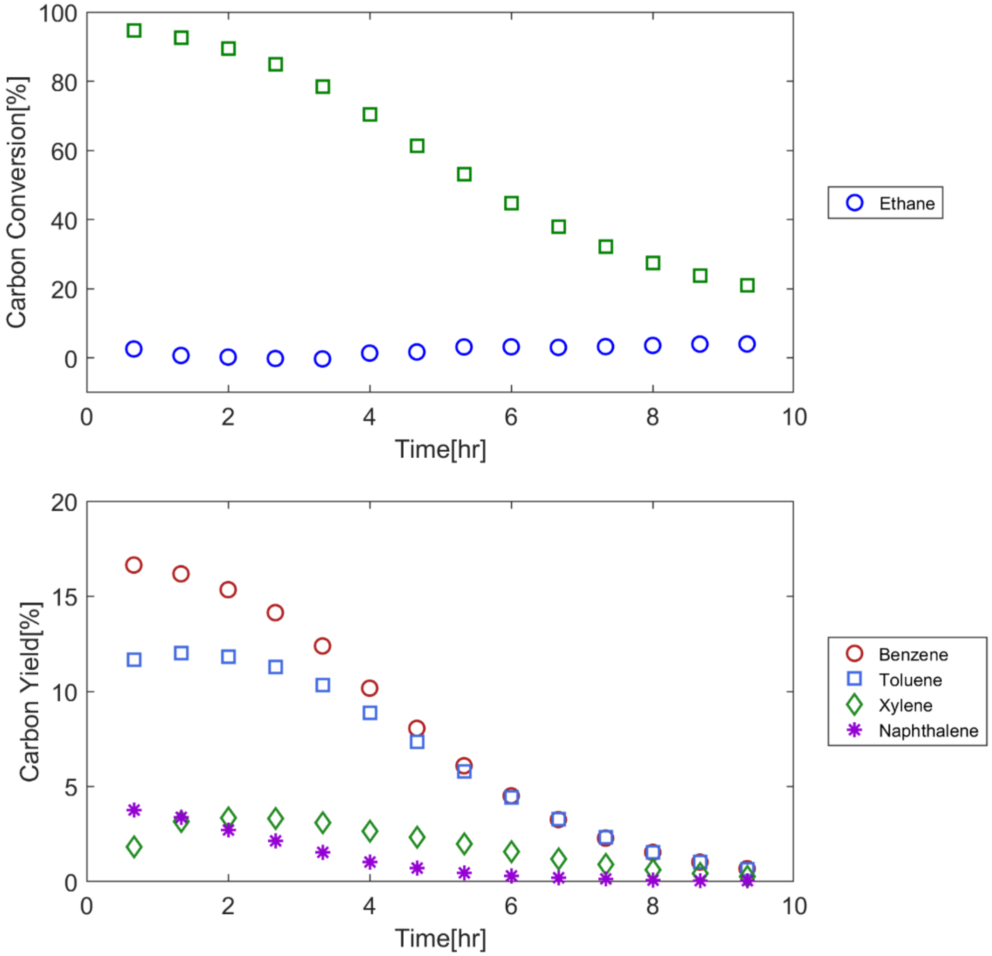

Figure 21 Experimental result of reactant conversion and product yield: N_2(6), C_2(3), C_3(3) at 600°C.

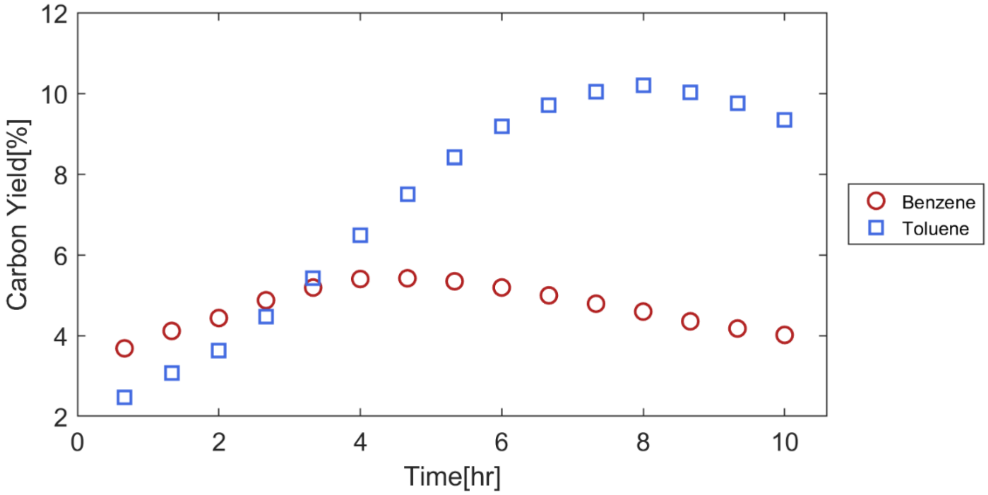

Figure 22 Experimental result of ethylene and propylene yield: N_2(6), C_2(0), C_3(6) at 600°C.

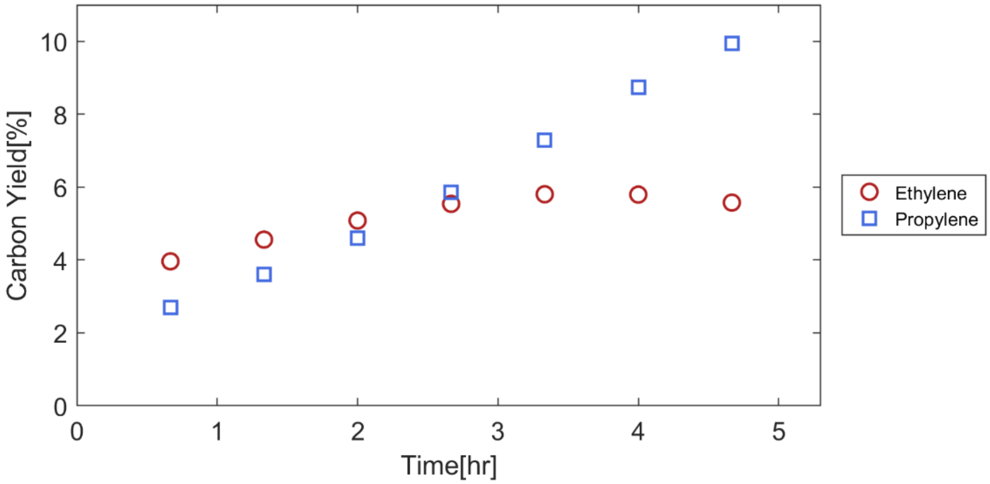

Figure 23 Experimental result of ethylene and propylene yield: N_2(8), C_2(0), C_3(4) at 600℃.

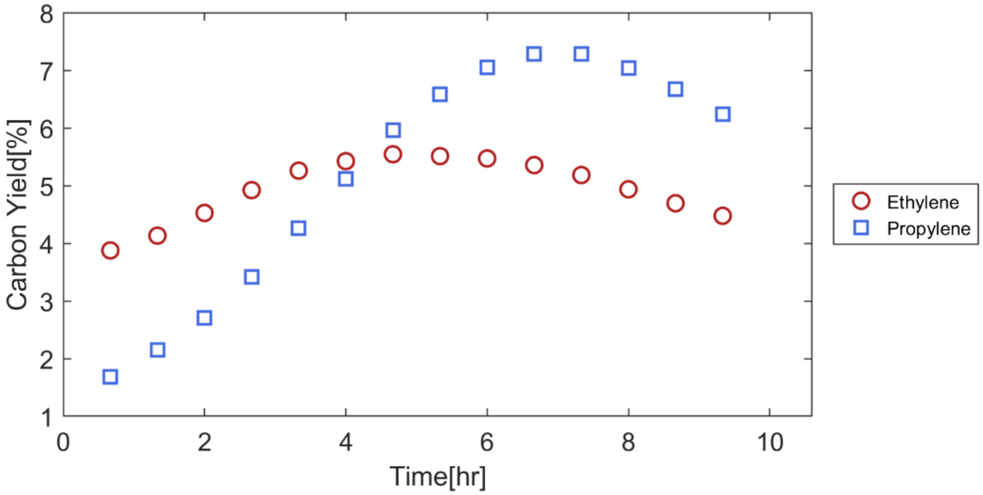

Figure 24 Experimental result of ethylene and propylene yield: N_2(6), C_2(3), C_3(3) at 600°C.

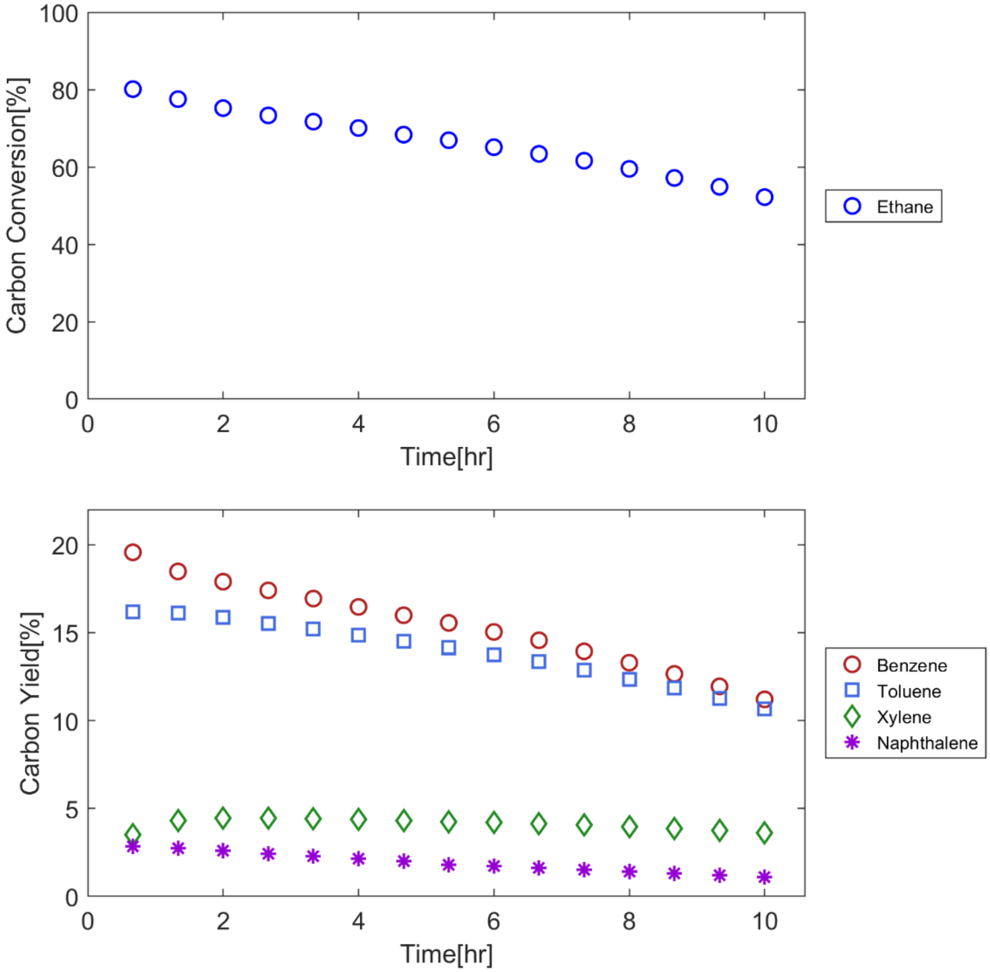

Figure 25 Experimental result of reactant conversion and product yield: N_2(6), C_2(0), C_3(6) at 550°C.

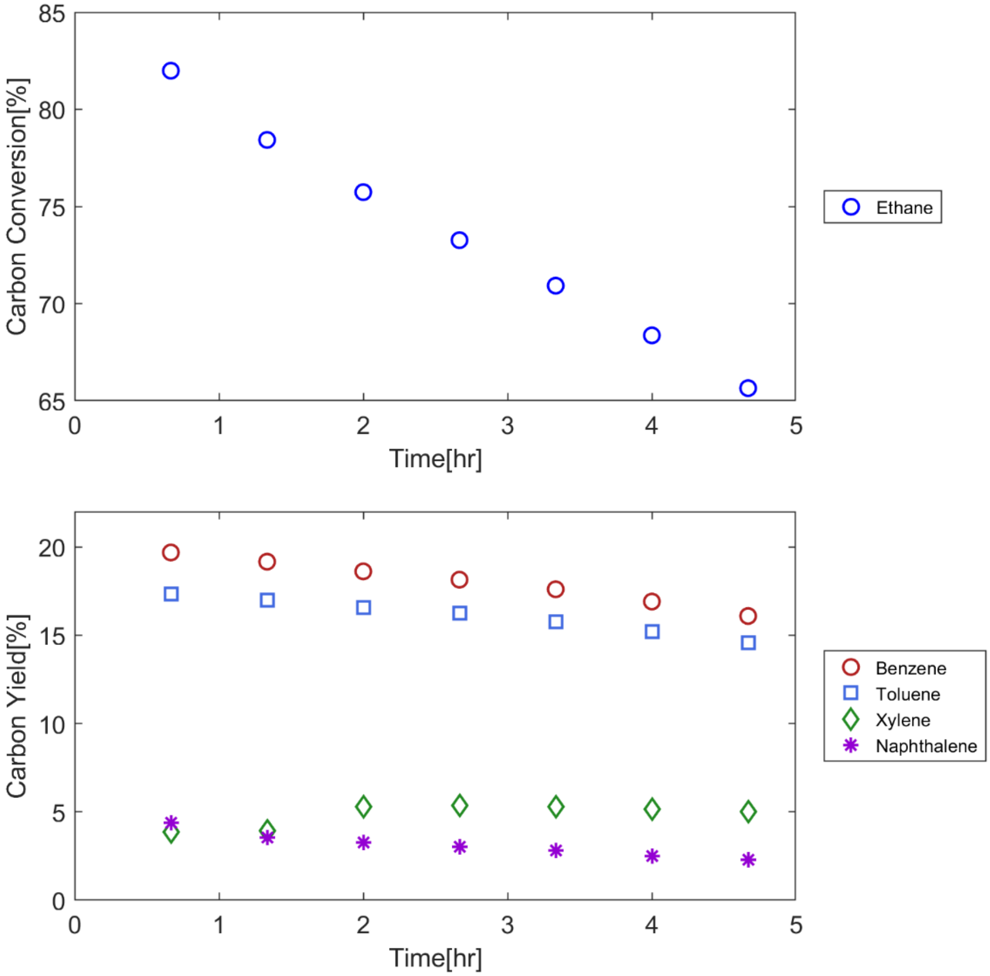

Figure 26 Experimental result of reactant conversion and product yield: N_2(8), C_2(0), C_3(4) at 550°C.

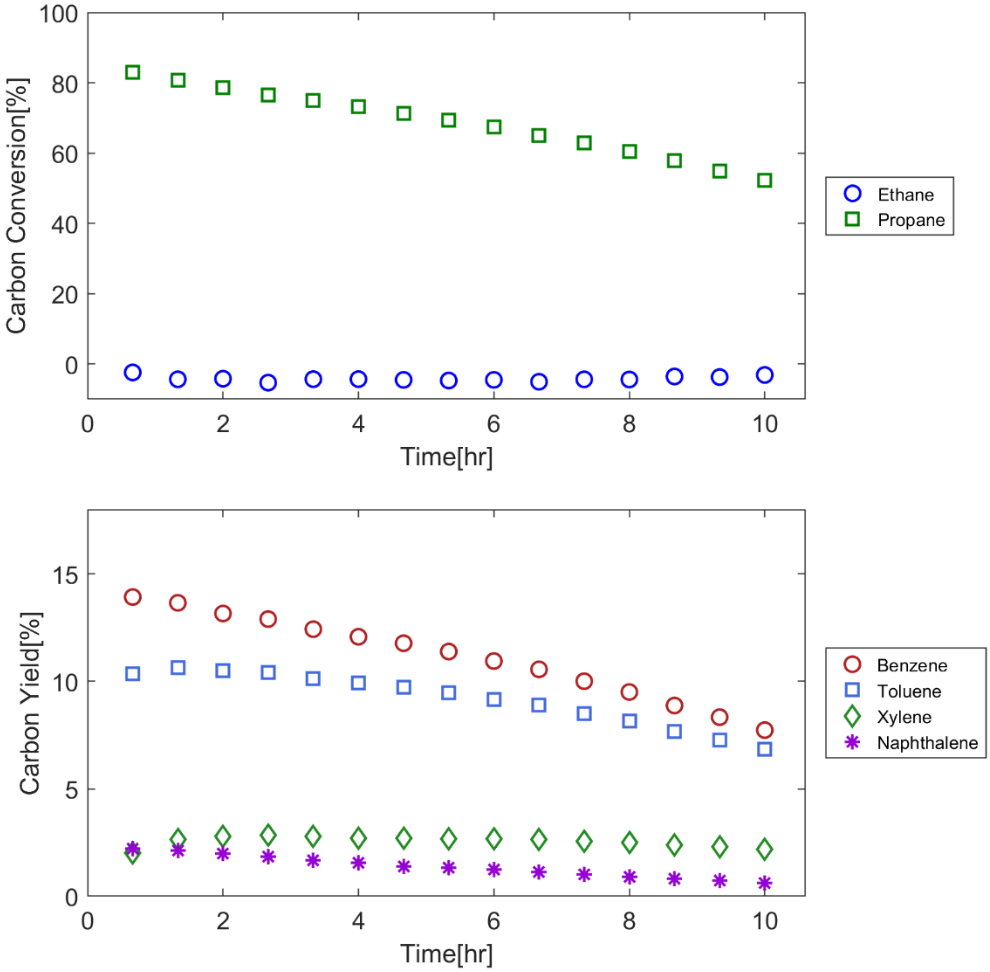

Figure 27 Experimental result of reactant conversion and product yield: N_2(6), C_2(3), C_3(3) at 550°C.

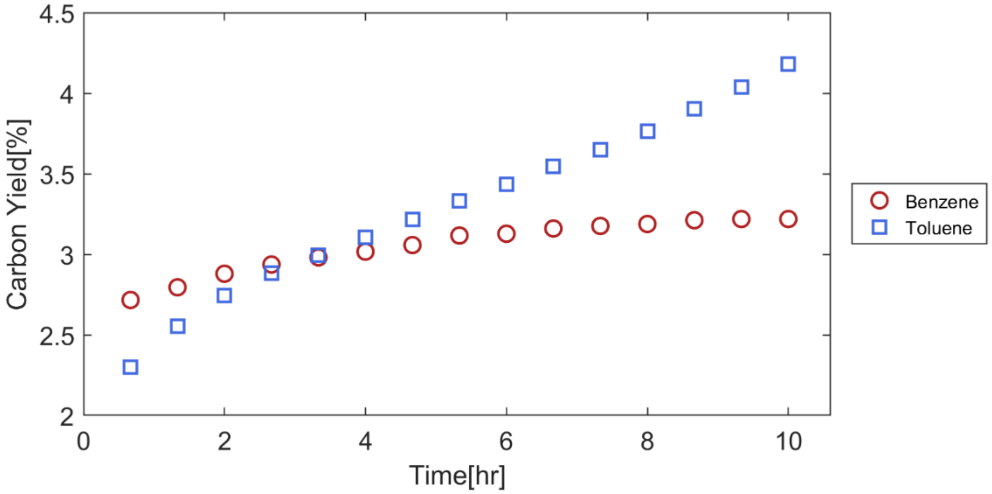

Figure 28 Experimental result of ethylene and propylene yield: N_2(6), C_2(0), C_3(6) at 550°C.

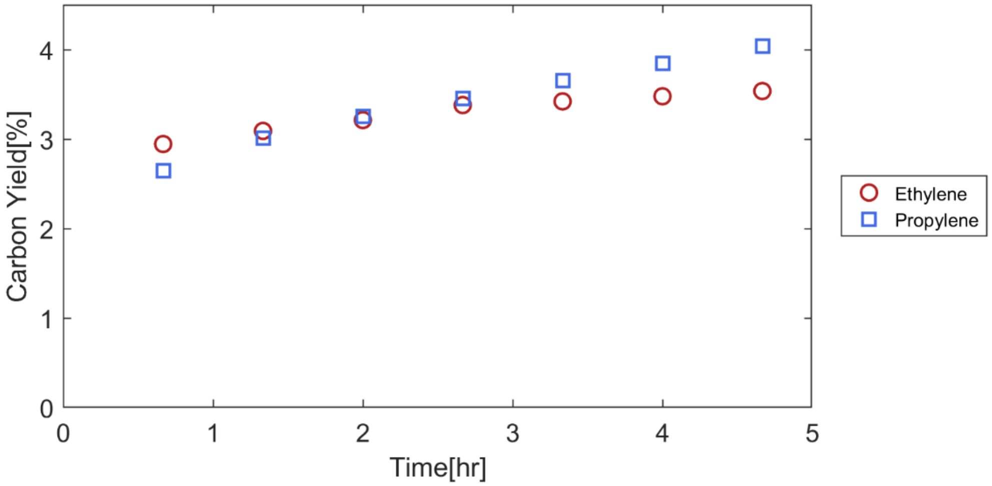

Figure 29 Experimental result of ethylene and propylene yield: N_2(8), C_2(0), C_3(4) at 550°C.

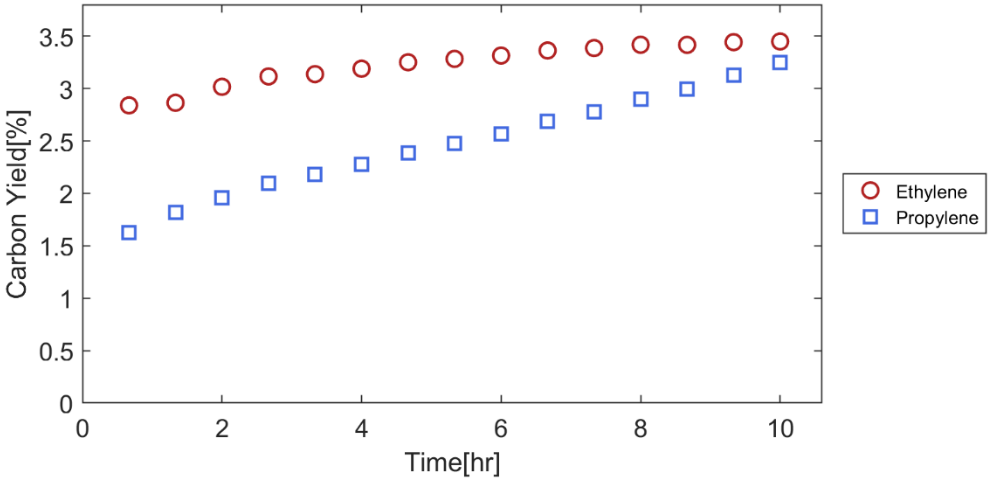

Figure 30 Experimental result of ethylene and propylene yield: N_2(6), C_2(3), C_3(3) at 550°C.

4.3. Result and Discussion

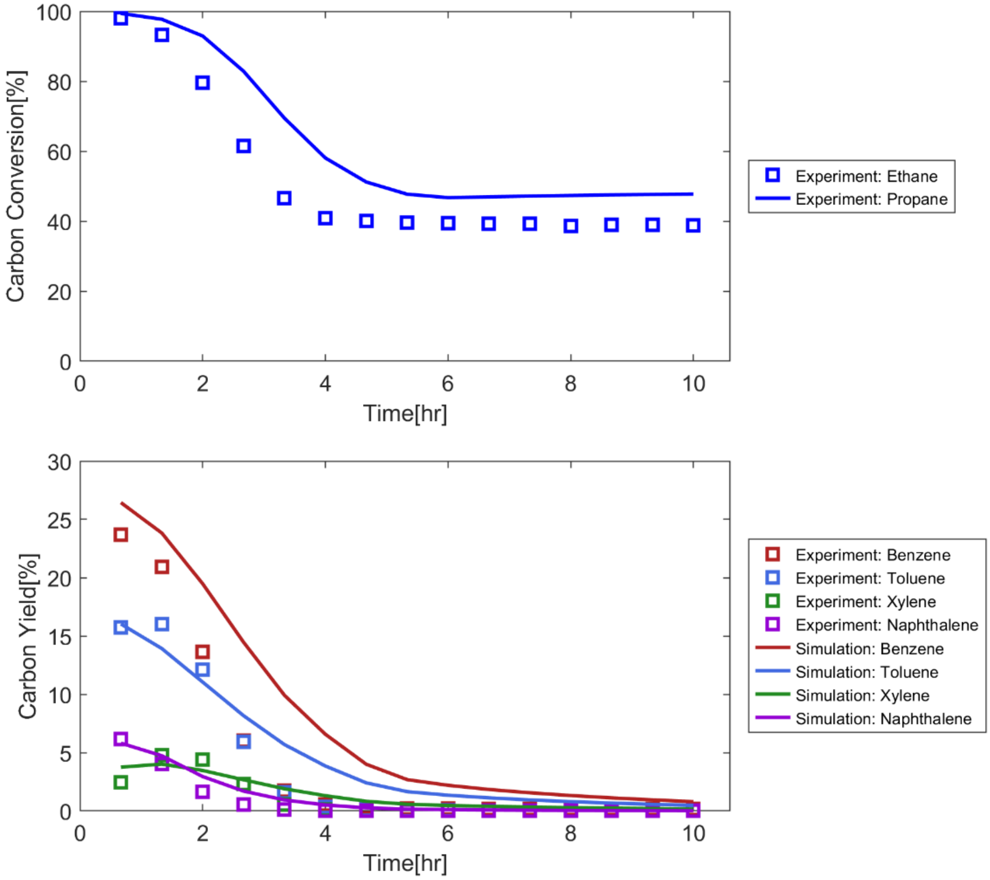

Figure 31 Comparison for reactant conversion and product yield of simulation result with experimental result: N_2(6), C_2(0), C_3(6), at 650℃

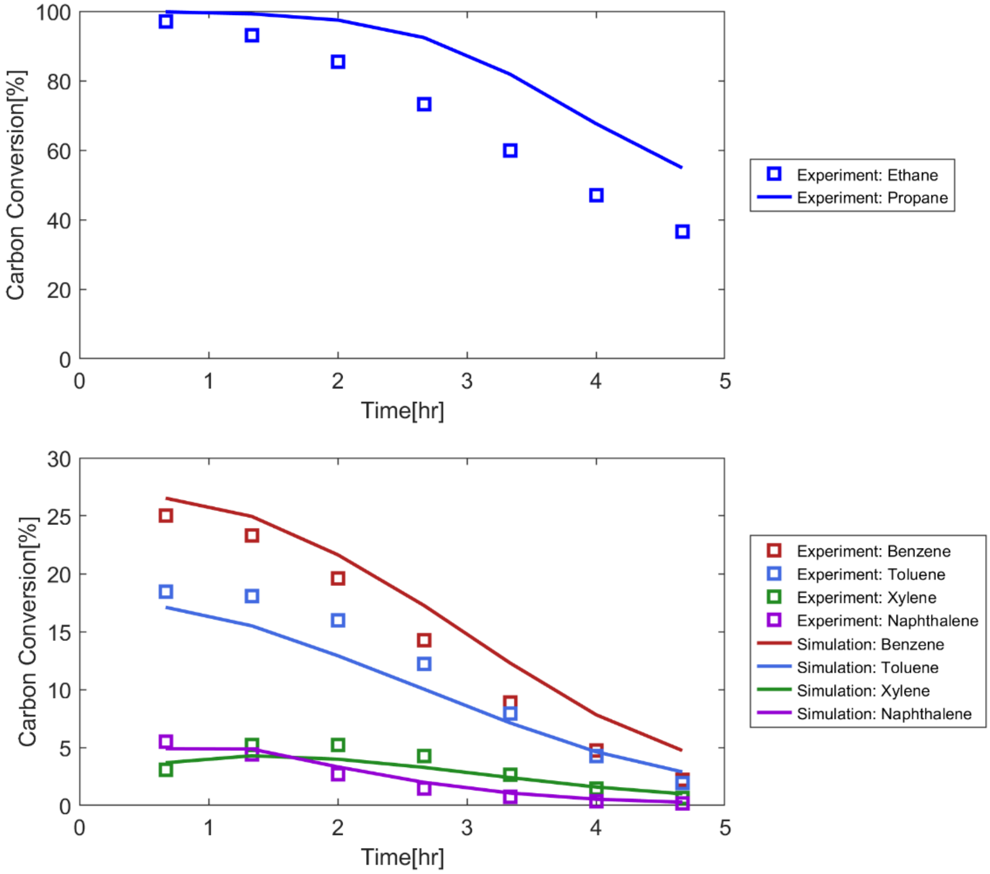

Figure 32 Comparison for reactant conversion and product yield of simulation result with experimental result: N_2(8), C_2(0), C_3(4), at 650℃

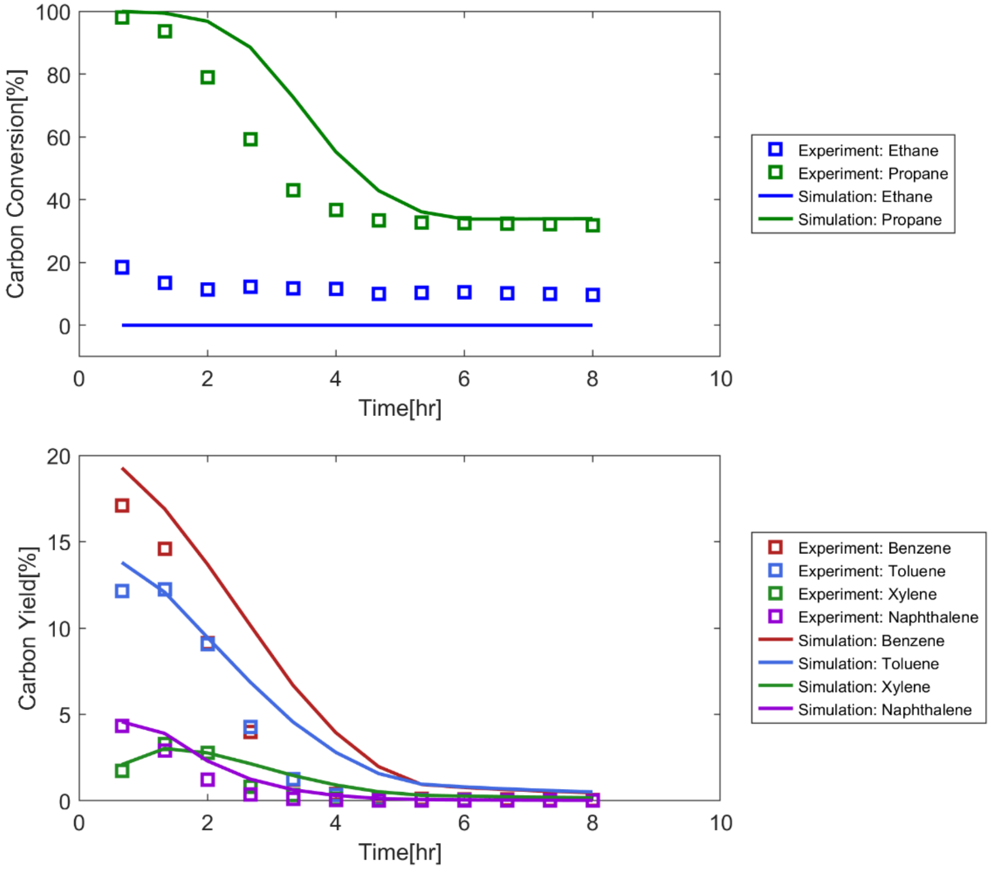

Figure 33 Comparison for reactant conversion and product yield of simulation result with experimental result: N_2(6), C_2(3), C_3(3), at 650℃

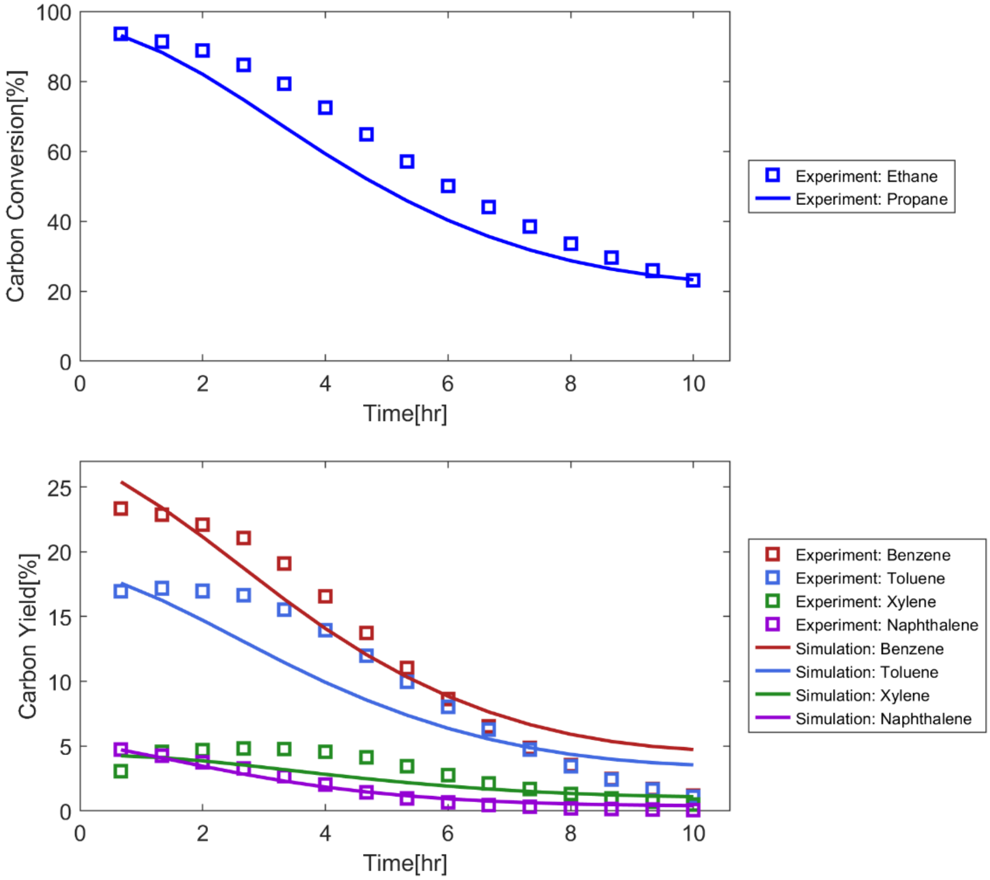

Figure 34 Comparison for reactant conversion and product yield of simulation result with experimental result: N_2(6), C_2(0), C_3(6), at 600℃.

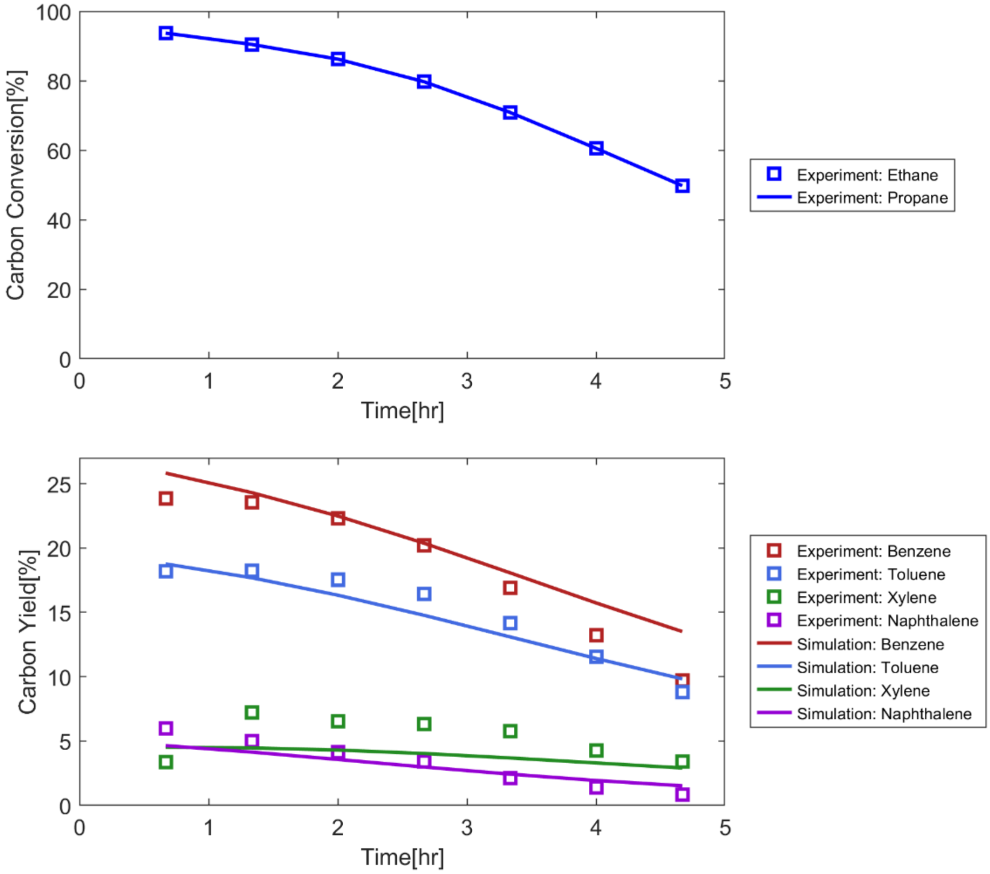

Figure 35 Comparison for reactant conversion and product yield of simulation result with experimental result: N_2(8), C_2(0), C_3(4), at 600℃.

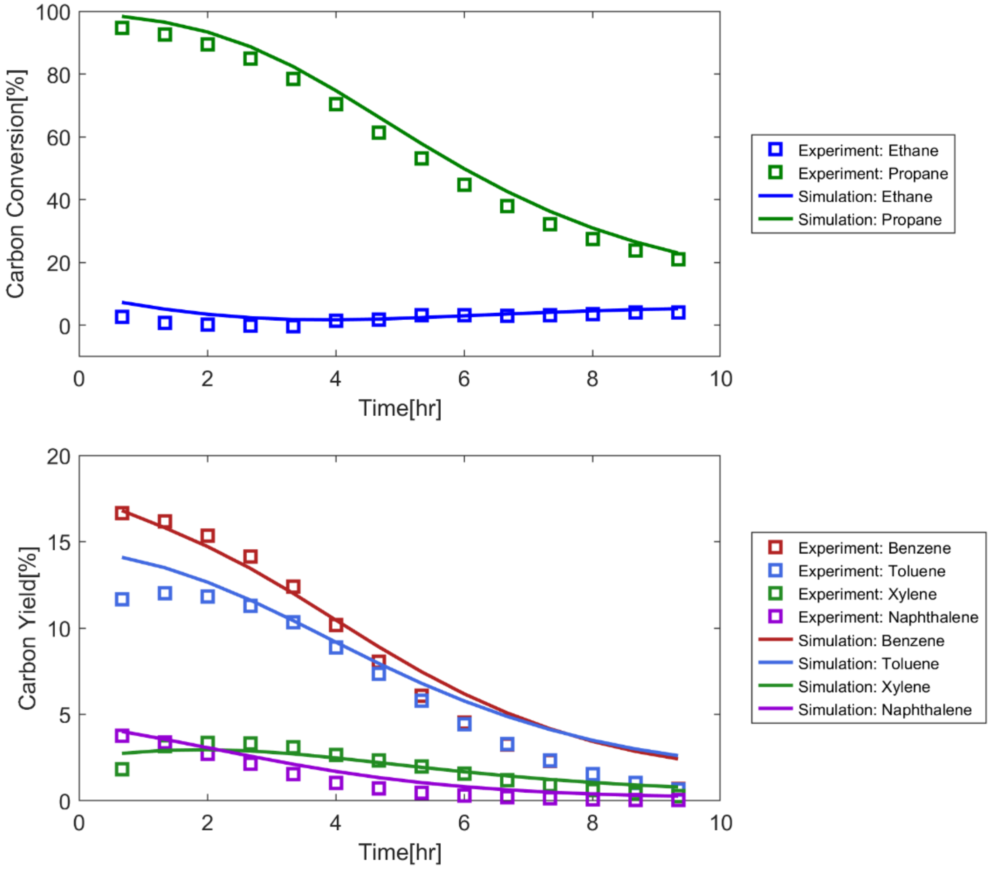

Figure 36 Comparison for reactant conversion and product yield of simulation result with experimental result: N_2(6), C_2(3), C_3(3), at 600℃.

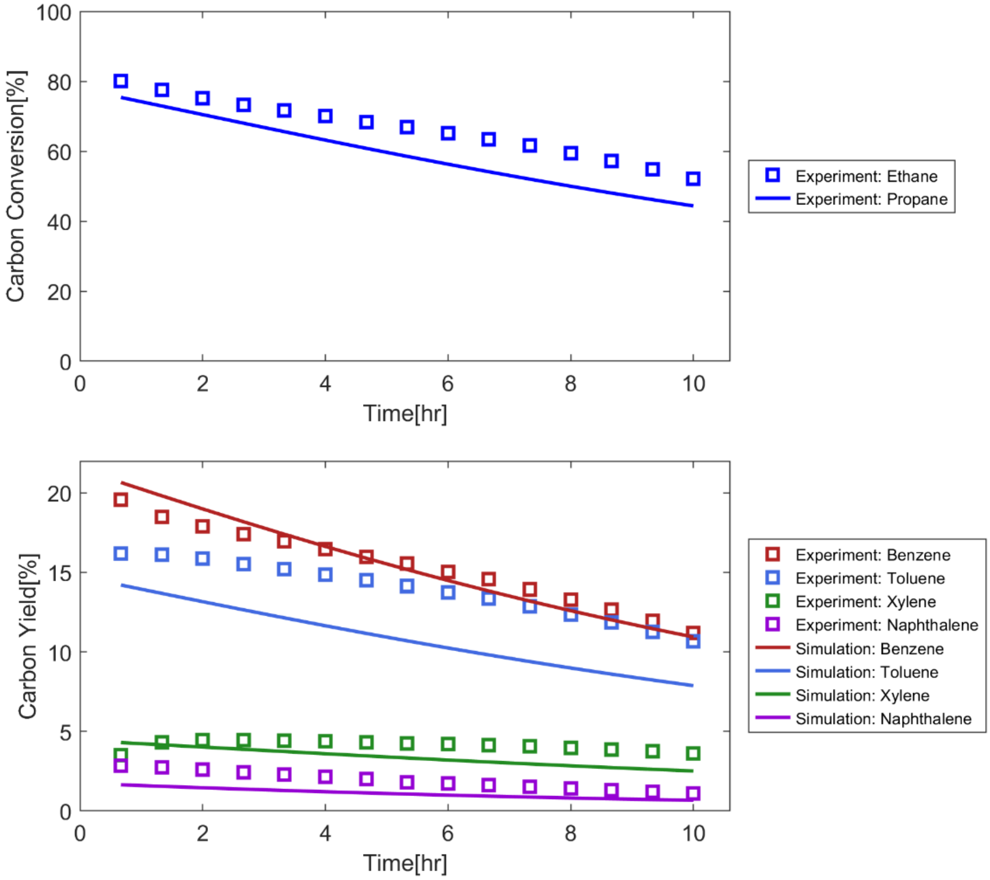

Figure 37 Comparison for reactant conversion and product yield of simulation result with experimental result: N_2(6), C_2(0), C_3(6), at 550℃.

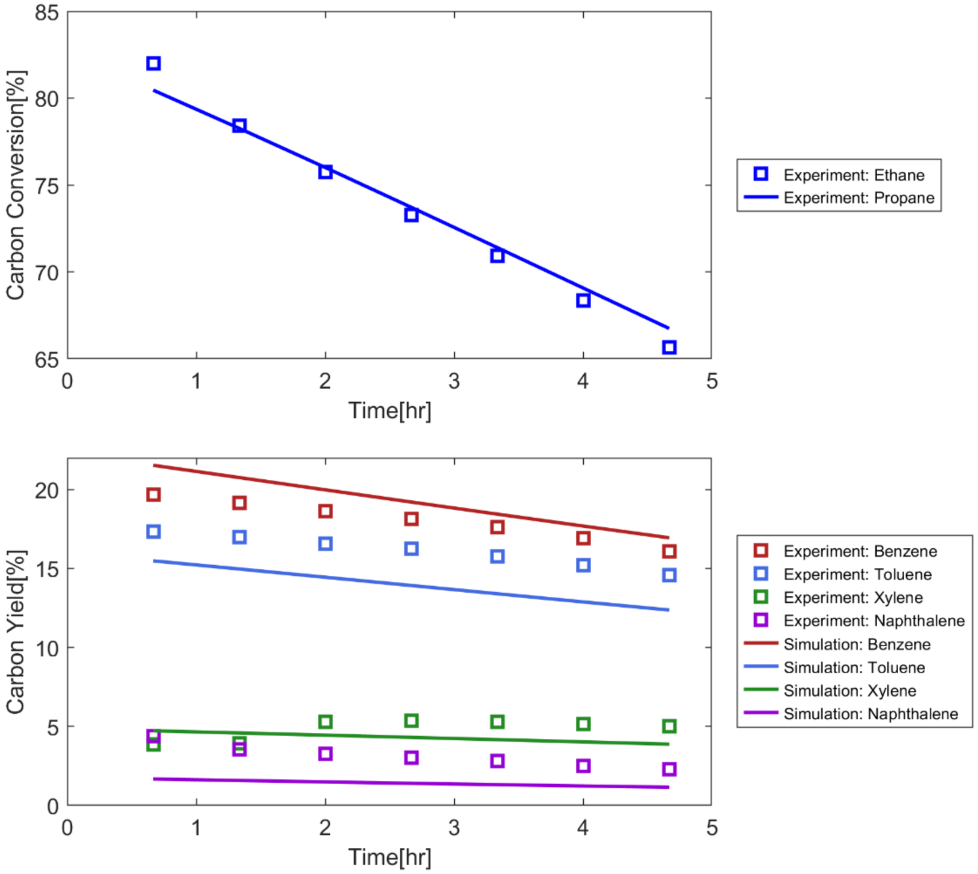

Figure 38 Comparison for reactant conversion and product yield of simulation result with experimental result: N_2(8), C_2(0), C_3(4), at 550°C.

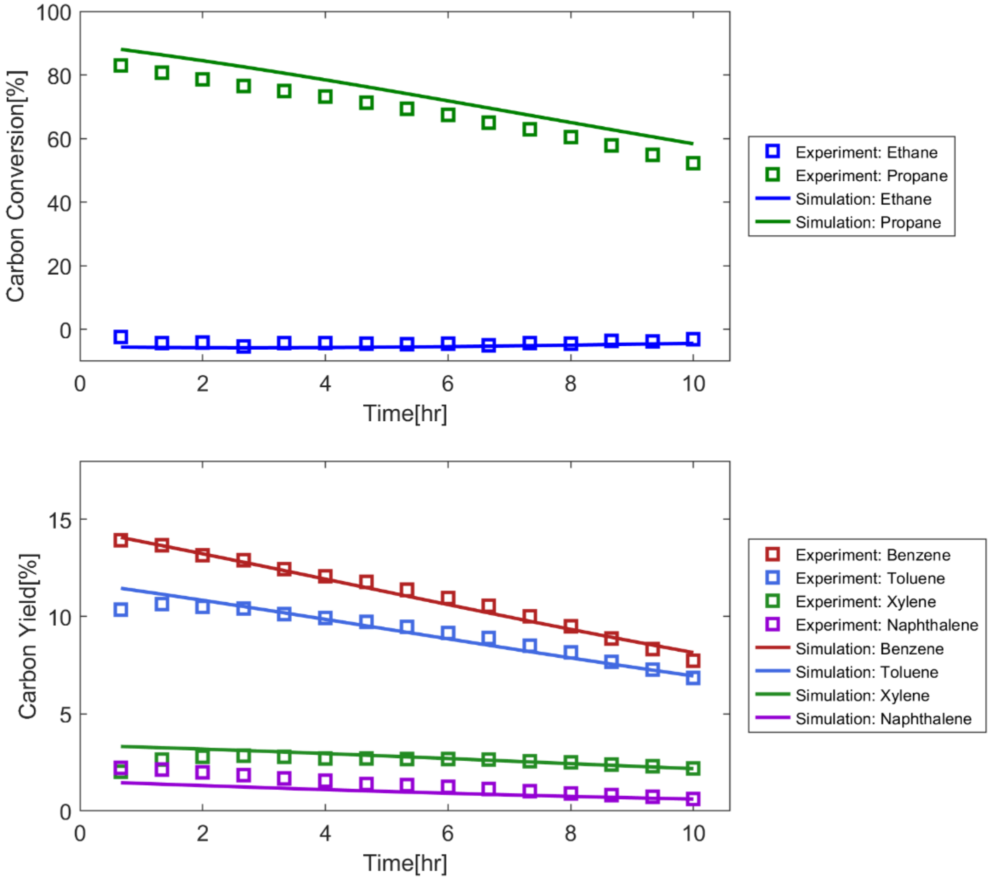

Figure 39 Comparison for reactant conversion and product yield of simulation result with experimental result: N_2(5), C_2(3), C_3(3), at 550°C.

Chapter 5. Concluding Remarks

5.1. Summary of Contributions

In the era of sustainability and green chemistry, various simulations have been conducted on catalytic reaction systems related to the conversion of important light hydrocarbons, such as Syngas and Shale gas, into valuable chemicals.

In Part II, it was analyzed that how the kinetics can change when transitioning from a single catalyst to a hybrid catalyst through the microkinetic modeling of the CZA/FER hybrid catalyst, integrating the reaction mechanisms of CZA and FER. Our group addressed the issue of predominance between the associative and dissociative paths in the controversial reaction of MeOH to DME in FER. Despite existing research suggesting the dominance of the Associative path in a standalone FER conversion system, this study suggested the possibility of the dissociative path dominating in the CZA/FER hybridization. The study proposed that this could be due to the facilitation of MeOH transfer from CZA to FER through hybridization, effectively increasing the partial pressure of MeOH.

In Part III, the system of ethane and propane aromatization reactions in Ga/ZSM-5 was developed using lumped kinetic modeling. During Part III, our group was able to selectively request experimental data needed for kinetic modeling through a joint research with the experimental team, successfully performing dynamic modeling of the catalytic deactivation of Ga/ZSM-5 in a long TOS of 10 hours. This is a major distinguishing factor from existing research typically conducted in less than 10 minutes TOS, or at most 3 hours. Also, referencing the kinetic mechanism reported by other researchers, we established oligomerization and coke formation kinetics without introducing C4 diene intermediates used in most research. We presented a simulation method that progresses deactivation differently in the LAS Ga-site and BAS H-site through site-separation for coke deposition. Based on these, we were able to relatively well predict the experimental results. Lastly, we successfully simulated the characteristic peak of the BTX yield curve observed in ethane and propane conversion experiments by introducing a mechanism where BTX is converted into cokes via naphthalene. The results of Part III are expected to provide meaningful reference materials for fellow researchers in the simulation of alkane oligomerization and catalyst deactivation in zeolites.

In summary, I propose that this research contributes in presenting various kinetic parameters for kinetic modeling, especially microkinetic modeling in catalytic conversion systems, and ideas for simulating catalysts exhibiting gradual deactivation.

5.2. Future Works

The catalytic conversion of shale gas to aromatics (BTX) over Mo/ZSM-5 is most suitable as future work. Shale gas is also a light hydrocarbon addressed in this study, and it is mainly composed of methane, a C1 chemical that is a key focus in green chemistry. Methane is extremely useful as a fuel, but as a fossil fuel, it has the drawback of emitting greenhouse gas CO2 as a combustion by-product, and methane itself is a potent greenhouse gas. Methane is also stored in considerable amounts as methane hydrate in the seabed and is abundantly distributed on Earth in the form of shale gas and natural gas. If we use this methane for the production of valuable products through catalytic conversion, it will be a tremendous contribution both chemically and environmentally.

Additionally, from the perspective of the primary scope of this study, kinetic modeling, there is the advantage of guaranteeing the cost-effectiveness of modeling, as a substantial part of the oligomerization reaction is shared with Ga/ZSM-5, which was modeled using lumped kinetics. Also, Mo/ZSM-5 is reported to show superior performance to Ga/ZSM-5 in overall catalyst activity, as a methyl radical is generated through adsorption reactions at the LAS Mo-site and is involved in the overall reaction. If we carry out microkinetic modeling composed of the elementary step reactions of this oligomerization mechanism, we believe we can obtain interesting and useful research results. We think that we can get good results if we perform DFT calculations for this research, or if we collaborate with a research team with the capability to do this research.

References

[1] J. Park, J. Cho, Y. Lee, M.-J. Park, and W. B. Lee, “Practical Microkinetic Modeling Approach for Methanol Synthesis from Syngas over a Cu-Based Catalyst,” *Ind Eng Chem Res*, vol. 58, no. 20, pp. 8663–8673, 2019, doi: 10.1021/acs.iecr.9b01254.

[2] R. D. Cortright and J. A. Dumesic, “Kinetics of heterogeneous catalytic reactions: Analysis of reaction schemes,” in *Advances in Catalysis*, Academic Press, 2001, pp. 161–264. doi: https://doi.org/10.1016/S0360-0564(02)46023-3.

[3] J. Park, J. Cho, M.-J. Park, and W. B. Lee, “Microkinetic modeling of DME synthesis from methanol over H-zeolite catalyst: Associative vs. dissociative pathways,” *Catal Today*, vol. 375, pp. 314–323, 2021, doi: 10.1016/j.cattod.2020.02.011.

[4] E. Shustorovich and H. Sellers, “The UBI-QEP method: A practical theoretical approach to understanding chemistry on transition metal surfaces,” *Surf Sci Rep*, vol. 31, no. 1, pp. 1–119, 1998, doi: https://doi.org/10.1016/S0167-5729(97)00016-2.

[5] G. Hetzer, P. Pulay, and H.-J. Werner, “Multipole approximation of distant pair energies in local MP2 calculations,” *Chem Phys Lett*, vol. 290, no. 1, pp. 143–149, 1998, doi: https://doi.org/10.1016/S0009-2614(98)00491-6.

[6] B. Hamed and A. Chad, “Development of Heterogeneous Catalysts for Dehydration of Methanol to Dimethyl Ether: A Review,” *Catal Ind*, vol. 11, no. 1, pp. 7–33, 2019, doi: 10.1134/s2070050419010045.

[7] J. R. Di Iorio, A. J. Hoffman, C. T. Nimlos, S. Nystrom, D. Hibbitts, and R. Gounder, “Mechanistic origins of the high-pressure inhibition of methanol dehydration rates in small-pore acidic zeolites,” *J Catal*, vol. 380, pp. 161–177, 2019, doi: 10.1016/j.jcat.2019.10.012.

[8] A. Brunetti, M. Migliori, D. Cozza, E. Catizzone, G. Giordano, and G. Barbieri, “Methanol conversion to dimethyl ether in catalytic zeolite membrane reactors,” *ACS Sustain Chem Eng*, vol. 8, no. 28, pp. 10471–10479, 2020.

[9] A. Trypolskyi, A. Zhokh, V. Gritsenko, M. Chen, J. Tang, and P. Strizhak, “A kinetic study on the methanol conversion to dimethyl ether over H-ZSM-5 zeolite,” *Chemical Papers*, vol. 75, no. 7, pp. 3429–3442, 2021, doi: 10.1007/s11696-021-01586-y.

[10] A. A. Rownaghi, F. Rezaei, and J. Hedlund, “Uniform mesoporous ZSM-5 single crystals catalyst with high resistance to coke formation for methanol deoxygenation,” *Microporous and Mesoporous Materials*, vol. 151, pp. 26–

33, 2012.

[11] L. C. Grabow and M. Mavrikakis, “Mechanism of Methanol Synthesis on Cu through CO2 and CO Hydrogenation,” *ACS Catal*, vol. 1, no. 4, pp. 365–384, 2011, doi: 10.1021/cs200055d.

[12] A. T. Aguayo, J. Ereña, D. Mier, J. M. Arandes, M. Olazar, and J. Bilbao, “Kinetic Modeling of Dimethyl Ether Synthesis in a Single Step on a CuO−ZnO−Al_2O_3/γ-Al_2O_3 Catalyst,” *Ind Eng Chem Res*, vol. 46, no. 17, pp. 5522–5530, 2007, doi: 10.1021/ie070269s.

[13] S. Fujita, S. Moribe, Y. Kanamori, M. Kakudate, and N. Takezawa, “Preparation of a coprecipitated Cu/ZnO catalyst for the methanol synthesis from CO2 — effects of the calcination and reduction conditions on the catalytic performance,” *Appl Catal A Gen*, vol. 207, no. 1, pp. 121–128, 2001, doi: https://doi.org/10.1016/S0926-860X(00)00616-5.

[14] H.-W. Lim, M.-J. Park, S.-H. Kang, H.-J. Chae, J. W. Bae, and K.-W. Jun, “Modeling of the Kinetics for Methanol Synthesis using Cu/ZnO/Al_2O_3/ZrO2 Catalyst: Influence of Carbon Dioxide during Hydrogenation,” *Ind Eng Chem Res*, vol. 48, no. 23, pp. 10448–10455, 2009, doi: 10.1021/ie901081f.

[15] R. Naumann d’Alnoncourt, X. Xia, J. Strunk, E. Löffler, O. Hinrichsen, and M. Muhler, “The influence of strongly reducing conditions on strong metal–support interactions in Cu/ZnO catalysts used for methanol synthesis,” *Physical Chemistry Chemical Physics*, vol. 8, no. 13, pp. 1525–1538, 2006, doi: 10.1039/B515487A.

[16] J. Park *et al.*, “Kinetic modeling for direct synthesis of dimethyl ether from syngas over a hybrid Cu/ZnO/Al_2O_3/ferrierite catalyst,” *Catal Today*, vol. 388–389, pp. 323–328, 2022, doi: 10.1016/j.cattod.2020.06.023.

[17] J. Skrzypek, M. Lachowska, and H. Moroz, “Kinetics of methanol synthesis over commercial copper/zinc oxide/alumina catalysts,” *Chem Eng Sci*, vol. 46, no. 11, pp. 2809–2813, 1991, doi: https://doi.org/10.1016/0009-2509(91)85150-V.

[18] G. H. Graaf, “The synthesis of methanol in gas-solid and gas-slurry reactors,” 1988.

[19] G. H. Graaf, E. J. Stamhuis, and A. A. C. M. Beenackers, “Kinetics of low-pressure methanol synthesis,” *Chem Eng Sci*, vol. 43, no. 12, pp. 3185–3195, 1988, doi: https://doi.org/10.1016/0009-2509(88)85127-3.

[20] G. H. Graaf, H. Scholtens, E. J. Stamhuis, and A. A. C. M. Beenackers, “Intra-particle diffusion limitations in low-pressure methanol synthesis,” *Chem Eng Sci*, vol. 45, no. 4, pp. 773–783, 1990, doi: https://doi.org/10.1016/0009-2509(90)85001-T.

[21] G. H. Graaf, P. J. J. M. Sijtsema, E. J. Stamhuis, and G. E. H. Joosten, “Chemical equilibria in methanol synthesis,” *Chem Eng Sci*, vol. 41, no. 11, pp. 2883–2890, 1986, doi: https://doi.org/10.1016/0009-2509(86)80019-7.

[22] S. Svelle, S. Kolboe, U. Olsbye, and O. Swang, “A Theoretical Investigation of the Methylation of Methylbenzenes and Alkenes by Halomethanes over Acidic Zeolites,” *J Phys Chem B*, vol. 107, no. 22, pp. 5251–5260, 2003, doi: 10.1021/jp030101u.

[23] P. G. Moses and J. K. Nørskov, “Methanol to Dimethyl Ether over ZSM-22: A Periodic Density Functional Theory Study,” *ACS Catal*, vol. 3, no. 4, pp. 735–745, 2013, doi: 10.1021/cs300722w.

[24] H. Xin *et al.*, “Catalytic dehydration of ethanol over post-treated ZSM-5 zeolites,” *J Catal*, vol. 312, pp. 204–215, 2014, doi: https://doi.org/10.1016/j.jcat.2014.02.003.

[25] A. H. Motagamwala and J. A. Dumesic, “Microkinetic Modeling: A Tool for Rational Catalyst Design,” *Chem Rev*, vol. 121, no. 2, pp. 1049–1076, 2021, doi: 10.1021/acs.chemrev.0c00394.

[26] A. Ghorbanpour, J. D. Rimer, and L. C. Grabow, “Computational assessment of the dominant factors governing the mechanism of methanol dehydration over H-ZSM-5 with heterogeneous aluminum distribution,” *ACS Catal*, vol. 6, no. 4, pp. 2287–2298, 2016.

[27] C. Karakaya, H. Zhu, and R. J. Kee, “Kinetic modeling of methane dehydroaromatization chemistry on Mo/Zeolite catalysts in packed-bed reactors,” *Chem Eng Sci*, vol. 123, pp. 474–486, 2015, doi: https://doi.org/10.1016/j.ces.2014.11.039.

[28] C. Karakaya, S. H. Morejudo, H. Zhu, and R. J. Kee, “Catalytic Chemistry for Methane Dehydroaromatization (MDA) on a Bifunctional Mo/HZSM-5 Catalyst in a Packed Bed,” *Ind Eng Chem Res*, vol. 55, no. 37, pp. 9895–9906, 2016, doi: 10.1021/acs.iecr.6b02701.

[29] A. Baz and A. Holewinski, “Understanding the interplay of bifunctional and electronic effects: Microkinetic modeling of the CO electro-oxidation reaction,” *J Catal*, vol. 384, pp. 1–13, 2020, doi: https://doi.org/10.1016/j.jcat.2020.02.003.

[30] F. Figueras, A. Nohl, L. de Mourgues, and Y. Trambouze, “Dehydration of methanol and tert-butyl alcohol on silica-alumina,” *Transactions of the Faraday Society*, vol. 67, no. 0, pp. 1155–1163, 1971, doi: 10.1039/TF9716701155.

[31] L. Kubelková, J. Nováková, and K. Nedomová, “Reactivity of surface species on zeolites in methanol conversion,” *J Catal*, vol. 124, no. 2, pp. 441–450, 1990, doi: https://doi.org/10.1016/0021-9517(90)90191-L.

[32] S. R. Blaszkowski and R. A. Van Santen, “The mechanism of dimethyl ether formation from methanol catalyzed by zeolitic protons,” *J Am Chem Soc*, vol. 118, no. 21, pp. 5152–5153, 1996, doi: 10.1021/ja954323k.

[33] S. R. Blaszkowski and R. A. van Santen, “Density Functional Theory Calculations of the Activation of Methanol by a Broensted Zeolitic Proton,” *J Phys Chem*, vol. 99, no. 30, pp. 11728–11738, 1995, doi: 10.1021/j100030a017.

[34] A. J. Jones and E. Iglesia, “Kinetic, Spectroscopic, and Theoretical Assessment of Associative and Dissociative Methanol Dehydration Routes in Zeolites,” *Angewandte Chemie International Edition*, vol. 53, no. 45, pp. 12177–12181, 2014, doi: https://doi.org/10.1002/anie.201406823.

[35] A. J. Jones, S. I. Zones, and E. Iglesia, “Implications of Transition State Confinement within Small Voids for Acid Catalysis,” *The Journal of Physical Chemistry C*, vol. 118, no. 31, pp. 17787–17800, 2014, doi: 10.1021/jp5050095.

[36] R. T. Carr, M. Neurock, and E. Iglesia, “Catalytic consequences of acid strength in the conversion of methanol to dimethyl ether,” *J Catal*, vol. 278, no. 1, pp. 78–93, 2011, doi: https://doi.org/10.1016/j.jcat.2010.11.017.

[37] T. Tagawab, G. Pleizier, and Y. Amenomiya, “Methanol synthesis from CO2+H2 I. characterization of catalysts by TPD,” *Appl Catal*, vol. 18, no. 2, pp. 285–293, 1985, doi: https://doi.org/10.1016/S0166-9834(00)84007-5.

[38] A. A. Gokhale, J. A. Dumesic, and M. Mavrikakis, “On the Mechanism of Low-Temperature Water Gas Shift Reaction on Copper,” *J Am Chem Soc*, vol. 130, no. 4, pp. 1402–1414, 2008, doi: 10.1021/ja0768237.

[39] N. Park, M.-J. Park, Y.-J. Lee, K.-S. Ha, and K.-W. Jun, “Kinetic modeling of methanol synthesis over commercial catalysts based on three-site adsorption,” *Fuel Processing Technology*, vol. 125, pp. 139–147, 2014, doi: 10.1016/j.fuproc.2014.03.041.

[40] D. Xu, P. Wu, and B. Yang, “Origin of CO 2 as the main carbon source in syngas-to-methanol process over Cu: theoretical evidence from a combined DFT and microkinetic modeling study,” *Catal Sci Technol*, vol. 10, no. 10, pp. 3346–3352, 2020.

[41] P. Wu and B. Yang, “Significance of surface formate coverage on the reaction kinetics of methanol synthesis from CO2 hydrogenation over Cu,” *ACS Catal*, vol. 7, no. 10, pp. 7187–7195, 2017.

[42] A. Prašnikar, D. L. Jurković, and B. Likozar, “Reaction path analysis of CO2 reduction to methanol through multisite microkinetic modelling over Cu/ZnO/Al2O3 catalysts,” *Appl Catal B*, vol. 292, p. 120190, 2021.

[43] C. T. Campbell, “Finding the Rate-Determining Step in a Mechanism:

Comparing DeDonder Relations with the ‘Degree of Rate Control,’” *J Catal*, vol. 204, no. 2, pp. 520–524, 2001, doi: https://doi.org/10.1006/jcat.2001.3396.

[44] C. T. Campbell, “The Degree of Rate Control: A Powerful Tool for Catalysis Research,” *ACS Catal*, vol. 7, no. 4, pp. 2770–2779, 2017, doi: 10.1021/acscatal.7b00115.

[45] C. T. Campbell, “Future Directions and Industrial Perspectives Micro- and macro-kinetics: Their relationship in heterogeneous catalysis,” *Top Catal*, vol. 1, no. 3, pp. 353–366, 1994, doi: 10.1007/BF01492288.

[46] D. Lin, D. Zhang, X. Zhang, B. M. Goncalves da Silva, L. Hu, and J. N. Meegoda, “Prediction of gas production rate from shale gas reservoirs using a micro–macro analysis,” *Sci Rep*, vol. 13, no. 1, p. 494, 2023, doi: 10.1038/s41598-023-27745-7.

[47] T. Muther *et al.*, “Unconventional hydrocarbon resources: geological statistics, petrophysical characterization, and field development strategies,” *J Pet Explor Prod Technol*, vol. 12, no. 6, pp. 1463–1488, 2022, doi: 10.1007/s13202-021-01404-x.

[48] X. Li, C. Pei, and J. Gong, “Shale gas revolution: Catalytic conversion of C1–C3 light alkanes to value-added chemicals,” *Chem*, vol. 7, no. 7, pp. 1755–1801, 2021, doi: https://doi.org/10.1016/j.chempr.2021.02.002.

[49] H. Chen, L. Li, and J. Hu, “Upgrading of stranded gas via non-oxidative conversion processes,” *Catal Today*, vol. 310, pp. 94–97, 2018, doi: https://doi.org/10.1016/j.cattod.2017.05.029.

[50] C. Zhang *et al.*, “Direct hydrogenation of CO2 into valuable aromatics over K/Fe-Cu-Al @HZSM-5 tandem catalysts: Effects of zeolite surface acidity on aromatics formation,” *Fuel Processing Technology*, vol. 248, p. 107824, 2023, doi: https://doi.org/10.1016/j.fuproc.2023.107824.

[51] A. Bhan and W. N. Delgass, “Propane Aromatization over HZSM-5 and Ga/HZSM-5 Catalysts,” *Catalysis Reviews*, vol. 50, no. 1, pp. 19–151, 2008, doi: 10.1080/01614940701804745.

[52] W. J. H. Dehertog and G. F. Fromen, “A catalytic route for aromatics production from LPG,” *Appl Catal A Gen*, vol. 189, no. 1, pp. 63–75, 1999, doi: https://doi.org/10.1016/S0926-860X(99)00252-5.

[53] P. Schwach, X. Pan, and X. Bao, “Direct Conversion of Methane to Value-Added Chemicals over Heterogeneous Catalysts: Challenges and Prospects,” *Chem Rev*, vol. 117, no. 13, pp. 8497–8520, 2017, doi: 10.1021/acs.chemrev.6b00715.

[54] I. Vollmer, I. Yarulina, F. Kapteijn, and J. Gascon, “Progress in Developing a Structure-Activity Relationship for the Direct Aromatization of Methane,”

ChemCatChem, vol. 11, no. 1, pp. 39–52, 2019, doi: https://doi.org/10.1002/cctc.201800880.

[55] Y. H. Lim, M. Y. Gim, H. Kim, and D. H. Kim, "Top-down HCl treatment to prepare highly active Ga species in Ga/ZSM-5 for propane aromatization," *Fuel Processing Technology*, vol. 227, p. 107107, 2022, doi: https://doi.org/10.1016/j.fuproc.2021.107107.

[56] B. S. Kwak, W. M. H. Sachtler, and W. O. Haag, "Catalytic Conversion of Propane to Aromatics: Effects of Adding Ga and/or Pt to HZSM-5," *J Catal*, vol. 149, no. 2, pp. 465–473, 1994, doi: https://doi.org/10.1006/jcat.1994.1313.

[57] D. Liu, L. Cao, G. Zhang, L. Zhao, J. Gao, and C. Xu, "Catalytic conversion of light alkanes to aromatics by metal-containing HZSM-5 zeolite catalysts—A review," *Fuel Processing Technology*, vol. 216, p. 106770, 2021, doi: https://doi.org/10.1016/j.fuproc.2021.106770.

[58] M. Raad, S. Hamieh, J. Toufaily, T. Hamieh, and L. Pinard, "Propane aromatization on hierarchical Ga/HZSM-5 catalysts," *J Catal*, vol. 366, pp. 223–236, 2018, doi: https://doi.org/10.1016/j.jcat.2018.07.035.

[59] C. Wang *et al.*, "Unraveling Hydrocarbon Pool Boosted Propane Aromatization on Gallium/ZSM-5 Zeolite by Solid-State Nuclear Magnetic Resonance Spectroscopy," *Angewandte Chemie International Edition*, vol. 60, no. 44, pp. 23630–23634, 2021, doi: https://doi.org/10.1002/anie.202111111.

[60] C. Liu *et al.*, "High Stability of Methanol to Aromatic Conversion over Bimetallic Ca,Ga-Modified ZSM-5," *ACS Catal*, vol. 12, no. 5, pp. 3189–3200, 2022, doi: 10.1021/acscatal.1c05481.

[61] P. He *et al.*, "Co-aromatization of methane with propane over Zn/HZSM-5: The methane reaction pathway and the effect of Zn distribution," *Appl Catal B*, vol. 250, pp. 99–111, 2019, doi: https://doi.org/10.1016/j.apcatb.2019.03.011.

[62] M. Guisnet and P. Magnoux, "Coking and deactivation of zeolites: Influence of the Pore Structure," *Appl Catal*, vol. 54, no. 1, pp. 1–27, 1989, doi: https://doi.org/10.1016/S0166-9834(00)82350-7.

[63] G. G. Oseke, A. Y. Atta, B. Mukhtar, B. Y. Jibril, and B. O. Aderemi, "Highly selective and stable Zn–Fe/ZSM-5 catalyst for aromatization of propane," *Appl Petrochem Res*, vol. 10, no. 2, pp. 55–65, 2020, doi: 10.1007/s13203-020-00245-9.

[64] I. B. Dauda *et al.*, "Highly Selective Hierarchical ZnO/ZSM-5 Catalysts for Propane Aromatization," *ACS Omega*, vol. 5, no. 6, pp. 2725–2733, 2020, doi: 10.1021/acsomega.9b03343.

[65] E. A. Pidko, E. J. M. Hensen, and R. A. van Santen, “Anionic Oligomerization of Ethylene over Ga/ZSM-5 Zeolite: A Theoretical Study,” *The Journal of Physical Chemistry C*, vol. 112, no. 49, pp. 19604–19611, 2008, doi: 10.1021/jp8069767.

[66] E. A. Uslamin, H. Saito, Y. Sekine, E. J. M. Hensen, and N. Kosinov, “Different mechanisms of ethane aromatization over Mo/ZSM-5 and Ga/ZSM-5 catalysts,” *Catal Today*, vol. 369, pp. 184–192, 2021, doi: https://doi.org/10.1016/j.cattod.2020.04.021.

[67] M. W. Schreiber *et al.*, “Lewis–Brønsted Acid Pairs in Ga/H-ZSM-5 To Catalyze Dehydrogenation of Light Alkanes,” *J Am Chem Soc*, vol. 140, no. 14, pp. 4849–4859, Apr. 2018, doi: 10.1021/jacs.7b12901.

[68] D. da Silva Fernandes, C. de Oliveira Veloso, and C. A. Henriques, “Propylene and aromatics from ethylene conversion over ZSM-5: Effect of zeolite composition,” *Catal Today*, vol. 381, pp. 108–117, 2021, doi: https://doi.org/10.1016/j.cattod.2020.08.014.

[69] L. H. Nguyen, T. Vazhnova, S. T. Kolaczkowski, and D. B. Lukyanov, “Combined experimental and kinetic modelling studies of the pathways of propane and n-butane aromatization over H-ZSM-5 catalyst,” *Chem Eng Sci*, vol. 61, no. 17, pp. 5881–5894, 2006, doi: https://doi.org/10.1016/j.ces.2006.05.017.